A Novel Dynamic Reliability-based Topology Optimization (DRBTO) Framework for Continuum Structures via Interval-process Collocation and the First-passage Theories

Lei Wang [a,b,c †], Yaru Liu [a], Dongliang Liu [a], Zhangming Wu [b]

a Institute of Solid Mechanics, School of Aeronautic Science and Engineering, Beihang University, Beijing 100083, China

b School of Engineering, Cardiff University, Newport Road 30-36, CF24 ODE, Cardiff, United Kingdom

c Aircraft and Propulsion Laboratory, Ningbo Institute of Technology, Beihang University, Ningbo 315100, China

[†]Corresponding author: Lei Wang. Email: ntucee.wanglei@gmail.com; leiwang_beijing@buaa.edu.cn

ABSTRACT

In view of the general inertia and damping features as well as the inevitable uncertainty factors in engineering structures, a novel dynamic reliability-based topology optimization (DRBTO) strategy is investigated for time-variant mechanical systems with overall consideration of material dispersion and loading deviation effects. The static interval-set model is first utilized to quantify multi-source uncertainty inputs and the transient interval-process model is then established to characterize unknown-but-bounded response results, which can be readily solved through the proposed interval-process collocation approach combined with a classical Newmark difference scheme. Differ from the traditional deterministic design framework, the present DRBTO scheme will directly consider new reliability constraints, for which the non-probabilistic time-variant reliability (NTR) index is mathematically deduced using the first-passage principle. In addition, the issues related to uncertainty-oriented design sensitivity and filtering method are discussed. The usage and effectiveness of DRBTO are demonstrated with three numerical examples.

Keywords: dynamic reliability-based topology optimization (DRBTO); the interval-process collocation; non-probabilistic time-variant reliability (NTR); the first-passage principle; uncertainty-oriented design sensitivity

1 Introduction

It is widely acknowledged that topology optimization (TO) is a powerful technology for material and structure system, due to its advantages of providing abundant space and flexible freedom in the design of material distribution [1, 2]. Most works so far have focused on the problems under static loads, but many structures are operated under time-varying load conditions. Compared with the prevailing static design, the inertia effect and time-dependent characteristic must be considered for the cases with high-frequency excitation. It remains challenging to handle the poor stability and slow convergence caused by the complex and nonlinear factors in dynamic analysis.

In view of different objective/constraint functions, the dynamic topology optimization (DTO) can be performed in both frequency domain and time domain. For the frequency domain based method, the basic frequency and frequency band are optimized to avoid sympathetic vibration [3]. Maeda et al. [4] designed vibrating structures and mechanical resonators with a multi-objective function in terms of eigenfrequencies, eigenmode shapes and stiffnesses in TO. Picelli et al. [5] maximized the fundamental eigenfrequency of acoustic–structure in considering of the coupling effects of fluid and structure interactions. However, these studies are not appropriate for the unsteady-state response optimization under non-harmonic or impact loads. Therefore, the maximum/mean dynamic performance [6, 7] are introduced to DTO. Min et al. [8] and Jang et al. [9] defined the energy natures of dynamic compliance and minimized it within a specified time interval or peaks interval using an equivalent static loads method. In addition, the dynamic response TO (DRTO) may also be applied in engineering applications [10-12]. Zhao et al. [13] developed an efficient way to reduce the maximum displacement over the complete vibration phase using the aggregation functional method and explored the influence of dynamic load and aggregation parameters. In general, the structural failure is not only related to the frequency, but also to the magnitude of external loads. Therefore, compared with the ordinary TO, applying the DTO method that is based on maximum dynamic responses is more comprehensive, however it is more challenge.

Most previous research works on DTO were carried out with deterministic assumptions, however, uncertain factors originating from external environmental disturbances and internal material imperfections are often inevitable [14-16]. The uncertainty-oriented approaches are divided into robust TO (RTO) [17] and reliability-based TO (RBTO) [18]. The RTO handles the uncertainties through constructing a comprehensive performance function in terms of their mean and standard deviation [19-21], while the RBTO brings the reliability theory, i.e.,

integrating the reliability index or failure probability, into the optimization framework [22, 23]. Obviously, more precise layout may be achieved using the RBTO strategy because the structural performance is measured to control the uncertainty influence in every iteration. In view of different uncertainty treatments, probabilistic model, fuzzy model, and convex model are established successively [24-26]. Meng et al. [27, 28] developed hybrid RTO and RBTO methods for epistemic and aleatory uncertainties. Bobby et al. [22] presented a simulation-based RBTO method for uncertain structures subject to stochastic excitation based on the first excursion probabilities. Zhao et al. [12] proposed a dynamic stress response reliability based topology optimization method for the design of multi-phase materials under random excitation. Sleesongsom et al. [29] established a multi-objective RBTO method based on a fuzzy set model, and an equivalent possibilistic safety index was defined along with mass, and compliance. In general, the distribution law and membership function of uncertainties cannot be acquired in many cases, which hinder the integration of probabilistic reliability and fuzzy reliability into the TO. Particularly, the non-probabilistic reliability first proposed by Ben Haim [30] approves that the system is convinced safe if the structure does not fail within the variation range of uncertainties. Luo [31] and Kang [32] modeled the uncertainties by multi-ellipsoid convex models and reformulated the nested optimization problem via the non-probabilistic reliability constraints on the concerned performance. Dos Santos et al. [33] decoupled the nested reliability optimization under stress constraints into a deterministic optimization step and a reliability analysis step by sequential optimization and reliability assessment.

Unfortunately, the time point where the maximum dynamic response occurs may vary significantly during the optimization process. Previous researches are mainly devoted efforts to the RBTO with static reliability indices [34], where the time-dependent characteristics of dynamic responses are ignored. To the best knowledge of the authors, little attention had been paid to DRTO method which is based on the non-probabilistic time-variant reliability (NTR). Nevertheless, the NTR assessment has been discussed thoroughly during recent decades. Jiang et al. [35] described the auto-covariance function and correlation coefficient function of variables at different times and established a NTR analysis method in the convex model process. Wang et al. [36] defined the NTR measurement considering interval uncertainties based on the first passage and the safety factor models. In addition, it has been wielded in other optimization problems successfully. Dubourg et al. [37] utilized the adaptive kriging metamodeling technique to surrogate the NTR functions and then adopted the subset simulation technique to analyze the reliability sensitivity. Fang et al. [38] presented a concept

of the equivalent most probable point (EMPP) and then transformed the NTR-based design into an equivalent time-invariant problem. Ma et al. [39] established a structural size and shape optimization model with dynamic reliability constraints. More excellent studies have been published in Refs. [40-42].

In this paper, a novel dynamic RBTO (DRBTO) approach with NTR constraints of dynamic response is elucidated for time-variant mechanical systems considering interval uncertainties. The rest of the paper is organized as follows. In Section 2, the basic problem of maximum DRTO is reviewed. The multi-source uncertainties are quantified by the static interval-set model and the transient interval-process model, and the collocation method is used to determine the interval-process of responses in Section 3. The framework of DRBTO and the NTR judgment based on the first-passage principle are expounded in Section 4. Section 5 presents our efficient methods for obtaining solutions, including sensitivity analysis, filtering method and overall procedures. The verification is eventually demonstrated by three numerical examples in Section 6. Conclusions are given in the last section.

2 Maximum dynamic response topology optimization (DRTO) problem under deterministic conditions

It had been widely accepted that the essence of structural TO lies in to find an optimal material/layout configuration under minimum weight ratio and satisfactory performance limitations. Commonly, the stiffness-based load-transferring path planning is a major concern in TO, and a traditional static TO process is formulated as,

$$\begin{aligned} &\min_{\chi} \ V = \int_{\mathbf{\Omega_d}} \chi(\zeta) d\zeta \\ &\text{s.t.} \ \ g(\zeta) \le \Gamma_{cri}, \ \text{if } \chi(\zeta) = 1 \\ &\qquad \chi(\zeta) = \begin{cases} 1, & \zeta \in \mathbf{\Omega_s} \\ 0, & \text{otherwise} \end{cases} \end{aligned} \tag{1}$$

where V is the total material volume with given design region $\mathbf{\Omega_d}$ and ζ denotes an arbitrary point located in $\mathbf{\Omega_d}$; $g(\zeta)$ means the actual response manifesting global/local structural stiffness and Γ_{cri} denotes the threshold; $\mathbf{\Omega_s} \subseteq \mathbf{\Omega_d}$ represents the domain occupied by solid materials.

In practical engineering, a structure always bears load conditions that are changing over time, and its dynamic response is further influenced by inertia and damping effects. Therefore, a TO design should also consider the transient characteristics in many typical cases, such as

vibration control, fatigue life extension, and anti-impact design. Under such circumstance, the above static 0-1 optimization model is no longer appropriate, and the following dynamic layout design framework which combines the finite element method (FEM) and the density-based updating strategy is explored, and given by,

$$\begin{aligned} &\min_{\rho_e} \ M = \sum_{e=1}^{NE} \rho_e V_e \\ &\text{s.t.} \ \ \mathbf{M}\ddot{\mathbf{u}}(t) + \mathbf{C}\dot{\mathbf{u}}(t) + \mathbf{K}\mathbf{u}(t) = \mathbf{f}(t) \\ &\qquad g_i\left(\rho_e,\ \mathbf{u}(t)\right) \le \Gamma_{i,cri} \\ &\qquad 0 < \underline{\rho} \le \rho_e \le 1, \quad 0 \le t \le T \\ &\qquad e = 1, 2, \cdots, NE, \quad i = 1, 2, \cdots, NC \end{aligned} \tag{2}$$

where the minimum mass term M is defined as the superposition of multiplicative results from the immediate density ρ_e and elemental volume V_e of each element; $\mathbf{M}$, $\mathbf{C}$ and $\mathbf{K}$ are the global mass, damping and stiffness matrices, respectively; g_i indicates the i-th time-varying performance function limited by the prescribed criterion $\Gamma_{i,cri}$; $\underline{\rho}$ is a positive lower bound assigned to design variables ρ_e ($e = 1, 2, \cdots, NE$) to avoid singularity of the stiffness matrix during the TO procedure; NE and NC are total numbers of finite elements and transient constraints. Note that during each layout iteration with initial conditions $\mathbf{u}(0) = \mathbf{u_0}$ and $\dot{\mathbf{u}}(0) = \dot{\mathbf{u}}_\mathbf{0}$, the displacement vector $\mathbf{u}(t)$, velocity vector $\dot{\mathbf{u}}(t)$ and acceleration vector $\ddot{\mathbf{u}}(t)$ can be obtained by solving the dynamic equilibrium equation.

To effectively tackle with the DRTO issue, the mapping relationship between the design variable and structural constitutive characteristics must be determined in advance. To prevent the appearance of the localized modes in dynamic analysis, the polynomial interpolation model improved by the standard SIMP model is incorporated in this study, i.e.,

$$\begin{aligned} E_e &= E_0\left(\alpha\eta_e^p + (1-\alpha)\eta_e\right) \\ \rho_e &= \rho_0\eta_e \end{aligned} \tag{3}$$

where E_0 and ρ_0 are the Young's modulus and structural density of the solid material, respectively; $\eta_e \in \left[\dfrac{\underline{\rho}}{\rho_0},\ 1\right]$ denotes the intermediate density; p ($p \ge 3$) is the so-called penalization factor; α is a positive real number that is close to but not greater than unity.

It is observed that there are different types of constraint functions (such as the dynamic compliance and the mean strain energy) reflecting time-variant structural stiffness behavior. With reference to local stiffness control problems, the nodal displacement monitoring of a

target degree of freedom (DOF) is the most obvious setting. Hence, associated with the interpolation law listed in Eq. (3), the lightweight design obtained by the maximum DRTO scheme (as illustrated in Fig. 1) arrives at

$$\begin{aligned} &\min_{\eta_e} \ M = \rho_0 \sum_{e=1}^{NE} \eta_e V_e \\ &\text{s.t.} \ \ \mathbf{M}(\eta_e)\ddot{\mathbf{u}}(t) + \mathbf{C}(\eta_e,\ E_e)\dot{\mathbf{u}}(t) + \mathbf{K}(E_e)\mathbf{u}(t) = \mathbf{f}(t) \\ &\qquad \mathbf{L}^T\mathbf{u}(t) \le u_{cri} \\ &\qquad E_e = E_0\left(\alpha\eta_e^p + (1-\alpha)\eta_e\right) \\ &\qquad \frac{\underline{\rho}}{\rho_0} \le \eta_e \le 1, \quad 0 \le t \le T \\ &\qquad e = 1, 2, \cdots, NE \end{aligned} \tag{4}$$

where $\mathbf{L}$ stands for the location vector with unity at the target DOF entry and are zeros elsewhere; u_{cri} means the allowable displacement.

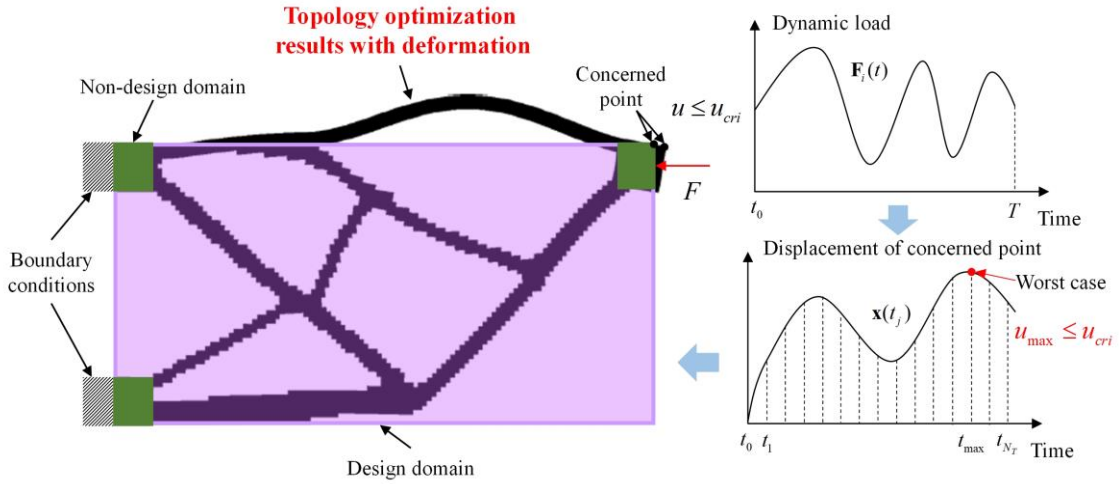

Fig. 1 Schematic diagram for maximum DRTO [43]

3 Interval quantification and propagation for time-variant mechanical systems

In practical engineering, parametric uncertainty factors (such as material dispersion, loading fluctuation, and principal deviation, etc.) are inevitable and obviously affect the mechanical behaviors, in particular, the time-variant stiffness feature $\mathbf{u}(t) = \left(u_i(t)\right)$. Hence, some initial property parameters are essentially uncertain variables and structural dynamic responses also have certain degrees of uncertainty rather than deterministic time histories. In view of this, how to reasonably consider multi-source uncertainty inputs and further guide a time-varying uncertainty propagation analysis is the key to complete the TO task.

3.1 Static interval-set and dynamic interval-process modeling

Owing to the sample insufficiency conditions in practice, the classical quantitative approaches based on the probability framework will no longer be feasible, therefore, the non-statistical quantitative description derived from the set theory is applied. For the sake of convenience, the following static interval vector [44, 45] denoted by $\mathbf{x}$ is defined and expressed as,

$$\mathbf{x} \in \mathbf{x}^{\mathbf{I}} = \left[x_1^I, x_2^I, ..., x_l^I \right]^T \quad \text{and} \quad x_j \in x_j^I = \left[\underline{x}_j,\ \overline{x}_j \right] \quad j = 1, 2, ..., l \tag{5}$$

where the superscript 'I' represents the interval set and the subscript 'l' denotes the uncertainty dimension. Then, one obtains that

$$\underline{\mathbf{x}} = \left[\underline{x}_1,\ \underline{x}_2,\ ...,\ \underline{x}_l \right]^T \quad \text{and} \quad \overline{\mathbf{x}} = \left[\overline{x}_1,\ \overline{x}_2,\ ...,\ \overline{x}_l \right]^T \tag{6}$$

Based on the interval mathematics, Eq. (5) can be rewritten as

$$\mathbf{x}^{\mathbf{I}} = \left[\underline{\mathbf{x}},\ \overline{\mathbf{x}} \right] = \left[\mathbf{x_0} - \mathbf{x_r},\ \mathbf{x_0} + \mathbf{x_r} \right] = \mathbf{x_0} + \mathbf{x_r} \circ \boldsymbol{\zeta} \tag{7}$$

where the Hadamard operator '$\circ$' stands for the corresponding entries in two multiplied vectors, and the vector $\boldsymbol{\zeta} = \left[\zeta_1,\ \zeta_2,\ ...,\ \zeta_l \right]^T$ encloses an l-dimensional standard interval set with $\zeta_j \in \left[-1,\ 1 \right]$. Hence, the mean value vector $\mathbf{x_0}$ as well as the radius vector $\mathbf{x_r}$ are given by,

$$\mathbf{x_0} = (x_{j,0}) = \frac{(\overline{\mathbf{x}} + \underline{\mathbf{x}})}{2} \quad \text{and} \quad \mathbf{x_r} = (x_{j,r}) = \frac{(\overline{\mathbf{x}} - \underline{\mathbf{x}})}{2} \tag{8}$$

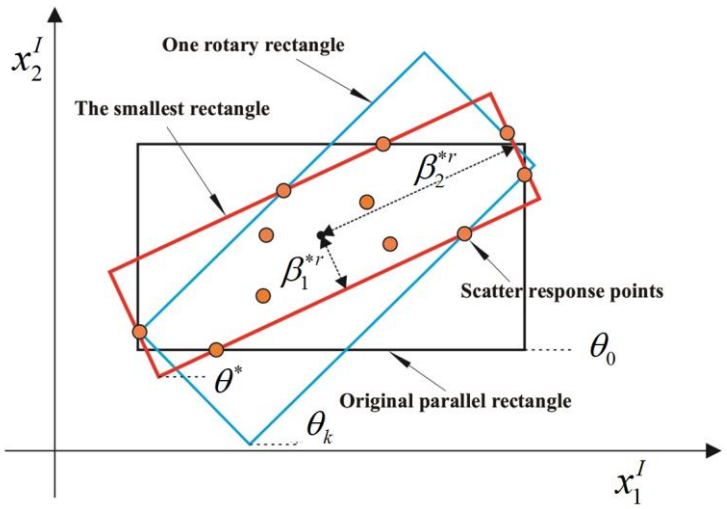

Fig. 2 Uncertainty quantification based on the smallest interval-set method

It is important to highlight that the elaborate quantification operation of lower and upper bounds of uncertain parameters, namely, the level of uncertainties, will be performed in advance based on some available static and dynamic sample data. In addition, some auxiliary

small-sample means, like the smallest interval-set method, gray systematic theory, information entropy technology, etc. [25, 46], are further involved to envelope the experimental data and determine the interval boundaries. For example, as shown in Fig. 2, the smallest rotary rectangular domain plotted in the orange domain is generated using optimization approaches in a two-dimensional sample space ($x_1^I - x_2^I$). Then, the final interval numbers β_1^* and β_2^* are used to replace the initial inputs x_1 and x_2 for the subsequent uncertainty propagation analysis.

Once the above uncertain parameters (including the material dispersion and loading deviation embodied by the static interval-set model) are taken into account in the dynamic systems, the nodal displacement responses will result in uncertain processes rather than specific time histories. In this case, the following interval-process model can be involved to characterize the time-varying uncertainty quantities, i.e.,

$$\mathbf{u}(\mathbf{x},\ t) = \left(u_i(\mathbf{x},\ t)\right) \in \mathbf{u}^{\hat{\mathbf{I}}}(\mathbf{x},\ t) = \left[\underline{\mathbf{u}}(\mathbf{x},\ t),\ \overline{\mathbf{u}}(\mathbf{x},\ t)\right], \quad 0 \le t \le T \tag{9}$$

where the superscript '$\hat{I}$' means the interval process. Similar with the representation of the interval set, vectors of the mean value process $\mathbf{u_0}(\mathbf{x},\ t)$ and the radius process $\mathbf{u_r}(\mathbf{x},\ t)$ can be analyzed as well.

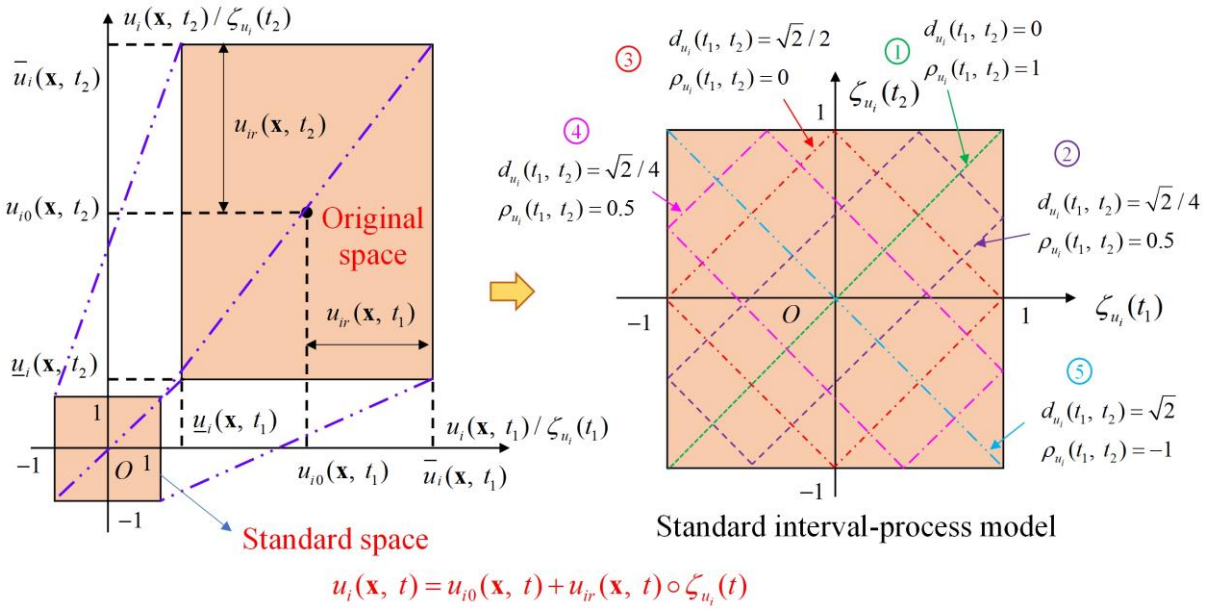

Fig. 3 The geometric logic for the time-varying interval process with correlation influences

Note that if $\mathbf{u_0}(\mathbf{x},\ t)$ and $\mathbf{u_r}(\mathbf{x},\ t)$ are known variables, the boundary rule of transient displacement process at any time can be directly revealed (degenerating into the static format). However, the time-dependency essence between two time-discretized response

results subjected to the target DOF $u_i(\mathbf{x},\ t_1)$ and $u_i(\mathbf{x},\ t_2)$ should be further discussed to precisely measure the feasible domain of $\mathbf{u}(\mathbf{x},\ t)$. Consequently, the auto-covariance function $\mathrm{Cov}_{u_i}(t_1,\ t_2)$ and the auto-correlation coefficient function $\rho_{u_i}(t_1,\ t_2)$ are defined in the following expression and meet the condition as,

$$\rho_{u_i}(t_1,\ t_2)=\left.\frac{\mathrm{Cov}_{u_i}(t_1,\ t_2)}{\sqrt{D_{u_i}(t_1)}\cdot\sqrt{D_{u_i}(t_2)}}\right|_{\mathbf{x}} \tag{10}$$

where the variance process vector yields

$$\mathbf{D}_{\mathbf{u_i}}(t)=\left(D_{u_i}(t)\right)\Big|_{\mathbf{x}}=\mathbf{u}_{\mathbf{r}}(\mathbf{x},\ t)\circ\mathbf{u}_{\mathbf{r}}(\mathbf{x},\ t) \tag{11}$$

As illustrated in Fig. 3, the geometric logic for description of the time-varying uncertain nature of $u_i(\mathbf{x},\ t_1)$ and $u_i(\mathbf{x},\ t_2)$ can be clearly exhibited in which the correlation index $\rho_{u_i}(t_1,\ t_2)$ satisfies

$$\rho_{u_i}(t_1,\ t_2)=1-\sqrt{2}d_{u_i}(t_1,\ t_2) \tag{12}$$

where $d_{u_i}(t_1,\ t_2)$ stands for the characteristic length in a normalized rotating rectangle. More details are provided in Appendix A.

3.2 Uncertain transient analysis based on the interval-process collocation theorem

As aforementioned, once the interval-set model $\mathbf{x}$ for quantifying initial static uncertainties is involved, the transient responses for each topology pattern will definitely not be deterministic time curves but may be changed versus certain ranges. Thereby, the dynamic equilibrium equation in Eq. (2) will be replaced by an interval process format, namely,

$$\mathbf{M}^{\mathbf{I}}(\mathbf{x},\ \eta_e)\ddot{\mathbf{u}}^{\widehat{\mathbf{I}}}(\mathbf{x},\ t)+\mathbf{C}^{\mathbf{I}}(\mathbf{x},\ \eta_e,\ E_e)\dot{\mathbf{u}}^{\widehat{\mathbf{I}}}(\mathbf{x},\ t)+\mathbf{K}^{\mathbf{I}}(\mathbf{x},\ E_e)\mathbf{u}^{\widehat{\mathbf{I}}}(\mathbf{x},\ t)=\mathbf{f}^{\widehat{\mathbf{I}}}(\mathbf{x},\ t) \tag{13}$$

where $\mathbf{u}^{\widehat{\mathbf{I}}}(\mathbf{x},\ t)$ contains the space-time accumulation nature of $\mathbf{x}$ in current layout design, and it can be depicted as $\mathbf{u}^{\widehat{\mathbf{I}}}(\mathbf{x},\ t)=\left[\min_{\mathbf{x}\in\mathbf{x}^{\mathbf{I}}}\{\mathbf{u}(\mathbf{x},\ t)\},\ \max_{\mathbf{x}\in\mathbf{x}^{\mathbf{I}}}\{\mathbf{u}(\mathbf{x},\ t)\}\right]$. Obviously, the time-varying bounds of $\mathbf{u}^{\widehat{\mathbf{I}}}(\mathbf{x},\ t)$ constitute an irregular domain and may not be solved analytically, and hence, high-precision, high-performance numerical solution methods are explored and applied. Herein, a dimension-by-dimension approach, which combines the orthogonal polynomial expansion and the interval-process collocation, is proposed.

According to Eq. (7), any implementation vector $\tilde{\mathbf{x}}_{\mathbf{j}}$ related to x_j is defined as

$$\tilde{\mathbf{x}}_{\mathbf{j}}=\mathbf{x}_{\mathbf{0}}+\mathbf{x}_{\mathbf{r}}\circ\tilde{\mathbf{v}}_{\mathbf{j}} \tag{14}$$

where $\tilde{\boldsymbol{\upsilon}}_{\mathbf{j}}=\left[0,\ 0,\ ...,\ \tilde{\upsilon}_j,\ 0,\ ...\right]^T$ and $\tilde{\upsilon}_j$ is assigned by specific sampling strategy. In order to approximately build the mapping relationship from $\mathbf{x}$ to $u_i(\mathbf{x},\ t)=\mathbf{L}^T\mathbf{u}(\mathbf{x},\ t)$, the Chebyshev orthogonal basis function is utilized and it gives,

$$C_m(\upsilon_j)=\cos\left(m\arccos(\upsilon_j)\right),\quad -1\le\upsilon_j\le 1 \tag{15}$$

where m is the order of the polynomial which denotes a nonnegative integer. Then, a series of orthogonal polynomials $\{C_m(\upsilon_j)\}$ is obtained with a weight function $1/\sqrt{1-(\upsilon_j)^2}$ and the recursive formula arrives at,

$$\begin{cases} C_0(\upsilon_j)=1; \\ C_1(\upsilon_j)=\upsilon_j; \\ \quad\vdots \\ C_{m+1}(\upsilon_j)=2\upsilon_j C_m(\upsilon_j)-C_{m-1}(\upsilon_j) \end{cases} \tag{16}$$

With the time-discretization idea ($t_k=k\Delta t,\ \Delta t=T/N_t$), the following truncated Chebyshev series $T_{i,r}(\upsilon_j,\ t_k)$ can be derived from

$$u_i(\mathbf{x}_{\mathbf{j}},\ t_k)=\mathbf{L}^T\mathbf{u}(\mathbf{x}_{\mathbf{j}},\ t_k)\approx T_{i,r}(\upsilon_j,\ t_k)=\frac{a_{0,i}(t_k)}{2}+\sum_{m=1}^{r}a_{m,i}(t_k)C_m(\upsilon_j) \tag{17}$$

where $\mathbf{x}_{\mathbf{j}}=\left[0,\ 0,\ ...,\ x_{j,0}+x_{j,r}\upsilon_j,\ 0,\ ...\right]^T$; $a_{m,i}(t_k)$ is calculated by [47]

$$a_{m,i}(t_k)=\frac{2}{\pi}\int_{-1}^{1}\frac{C_m(\upsilon_j)u_i(\tilde{\mathbf{x}}_{\mathbf{j}},\ t_k)}{\sqrt{1-(\upsilon_j)^2}}d\upsilon_j,\quad m=0,1,...,r \tag{18}$$

Considering the Gauss-Chebyshev quadrature formula, Eq. (18) is further converted by

$$a_{m,i}(t_k)\approx\frac{2}{\pi}\sum_{s=1}^{Nq}A_s C_m(\tilde{\upsilon}_{j,s})u_i(\tilde{\mathbf{x}}_{\mathbf{j,s}},\ t_k) \tag{19}$$

where $\tilde{\upsilon}_{j,s}$ ($s=1,2,\cdots,Nq$) represent Nq quadrature nodes that are the zero roots of $C_m(\upsilon_j)$; and one may have

$$\tilde{\mathbf{x}}_{\mathbf{j,s}}=\mathbf{x}_{\mathbf{0}}+\mathbf{x}_{\mathbf{r}}\circ\tilde{\boldsymbol{\upsilon}}_{\mathbf{j,s}}\qquad\text{and}\qquad A_s=\int_{-1}^{1}\frac{C_{Nq}(\upsilon_j)}{\sqrt{1-(\upsilon_j)^2}(\upsilon_j-\tilde{\upsilon}_{j,s})C_{Nq}{}'(\upsilon_j)}d\upsilon_j=\frac{\pi}{Nq} \tag{20}$$

Substituting Eqs. (19)-(20) into Eq. (17) yields

$$u_i(\mathbf{x}_{\mathbf{j}},\ t_k)\approx\frac{1}{Nq}\sum_{s=1}^{Nq}u_i(\tilde{\mathbf{x}}_{\mathbf{j,s}},\ t_k)+\frac{2}{Nq}\sum_{m=1}^{r}\sum_{s=1}^{Nq}u_i(\tilde{\mathbf{x}}_{\mathbf{j,s}},\ t_k)C_m(\tilde{\upsilon}_{j,s})C_m(\upsilon_j) \tag{21}$$

Apparently, once the explicit expression of Eq. (21) is available, the boundary conditions can be easily obtained by

$$\begin{cases} \underline{u}_i(\mathbf{x_j},\ t_k) = \min\limits_{\upsilon_j \in \Theta_j} \left\{ u_i(\mathbf{x_j},\ t_k) \right\} = u_i(\tilde{\mathbf{x}}_{\mathbf{j,min}},\ t_k) \\ \overline{u}_i(\mathbf{x_j},\ t_k) = \max\limits_{\upsilon_j \in \Theta_j} \left\{ u_i(\mathbf{x_j},\ t_k) \right\} = u_i(\tilde{\mathbf{x}}_{\mathbf{j,max}},\ t_k) \end{cases} \tag{22}$$

where $\Theta_j = \left\{ -1,\ 1,\ \dfrac{\partial T_{i,r}(\upsilon_j,\ t_k)}{\partial \upsilon_j} = 0 \right\}$; $\tilde{\mathbf{x}}_{\mathbf{j,min}}$ and $\tilde{\mathbf{x}}_{\mathbf{j,max}}$ respectively correspond to the extremum formula, i.e.,

$$\begin{cases} \tilde{\mathbf{x}}_{\mathbf{j,min}} = \left[x_{1,0},\ x_{2,0},\ ...,\ x_{j,0} + x_{j,r}\upsilon_{j,\min},\ ...,\ x_{l,0} \right]^T \Big|_{\upsilon_{j,\min} \in \Theta_j} \\ \tilde{\mathbf{x}}_{\mathbf{j,max}} = \left[x_{1,0},\ x_{2,0},\ ...,\ x_{j,0} + x_{j,r}\upsilon_{j,\max},\ ...,\ x_{l,0} \right]^T \Big|_{\upsilon_{j,\max} \in \Theta_j} \end{cases} \tag{23}$$

By traversing all cases of $\mathbf{x_j}$ and t_k, the lower and upper bounds of concerned nodal displacement history $u_i(\mathbf{x},\ t)$ can be eventually given by

$$u_i(\mathbf{x},\ t) \in \mathbf{L}^T \left[\underline{\mathbf{u}}(\mathbf{x},\ t),\ \overline{\mathbf{u}}(\mathbf{x},\ t) \right] \approx \left[u_i(\tilde{\mathbf{x}}_{\mathbf{min}},\ t),\ u_i(\tilde{\mathbf{x}}_{\mathbf{max}},\ t) \right] \tag{24}$$

where

$$\begin{cases} \tilde{\mathbf{x}}_{\mathbf{min}} = \mathbf{x_0} + \mathbf{x_r} \circ \left[\upsilon_{1,\min},\ \upsilon_{2,\min},\ \cdots,\ \upsilon_{l,\min} \right]^T \\ \tilde{\mathbf{x}}_{\mathbf{max}} = \mathbf{x_0} + \mathbf{x_r} \circ \left[\upsilon_{1,\max},\ \upsilon_{2,\max},\ \cdots,\ \upsilon_{l,\max} \right]^T \end{cases} \tag{25}$$

As stated in above, boundary rules of the dynamic uncertainty propagation from $\mathbf{x}$ to $u_i(\mathbf{x},\ t)$ can be mathematically revealed. With reference to the time-dependency properties for interval process $u_i(\mathbf{x},\ t)$, the first-order perturbation approach can be further incorporated to solve the auto-correlation coefficient function $\rho_{u_i}(t_{k-1},\ t_k)$ under linear hypothesis. Then, one may obtain

$$\rho_{u_i}(t_{k-1},\ t_k) \approx \frac{\sum\limits_{j=1}^{l} \left[\dfrac{\partial u_i(\mathbf{x_0},\ t_{k-1})}{\partial x_{j,0}(\ t_{k-1})} \cdot \dfrac{\partial u_i(\mathbf{x_0},\ t_k)}{\partial x_{j,0}(\mathbf{x_0},\ t_k)} \cdot x_{j,r}(\ t_{k-1}) \cdot x_{j,r}(\ t_k) \cdot \rho_{x_j}(t_{k-1},\ t_k) \right]}{\sqrt{\sum\limits_{j=1}^{l} \left[\left(\dfrac{\partial u_i(\mathbf{x_0},\ t_{k-1})}{\partial x_{j,0}} \cdot x_{j,r} \right)^2 \right]} \cdot \sqrt{\sum\limits_{j=1}^{l} \left[\left(\dfrac{\partial u_i(\mathbf{x_0},\ t_k)}{\partial x_{j,0}} \cdot x_{j,r} \right)^2 \right]}} \tag{26}$$

in which the partial derivatives can be calculated by differential strategy. For material properties, $x_{j,0}(\ t_{k-1}) = x_{j,0}(\mathbf{x_0},\ t_k) = x_{j,0}$, $x_{j,r}(\ t_{k-1}) = x_{j,r}(\ t_k) = x_{j,r}$, and $\rho_{x_j}(t_{k-1},\ t_k) = 1$, while for external forces, $x_{j,0}(\ t_{k-1})$, $x_{j,0}(\mathbf{x_0},\ t_k)$, $x_{j,r}(\ t_{k-1})$ and $x_{j,r}(\ t_k)$ may be determined by time discretization, and $\rho_{x_j}(t_{k-1},\ t_k)$ may be defined in advance or calculated by sequence auto-correlation based algorithm.

To sum up, all the characteristic variables for describing uncertain displacement histories can be achieved during each updating process of the topology structure. Namely, the correspondence between initial static uncertainties (quantified by the interval-set model $\mathbf{x}$) and final dynamic uncertainties (modeled by the interval process $u_i(\mathbf{x},\ t)$) is explicitly built, and the subsequent uncertainty-oriented safety evaluation and DRTO issues can be well tackled.

4 Dynamic reliability-based topology optimization (DRBTO)

4.1 Reliability-oriented optimization formulation

As stated in Section 3, once the unknown-but-bounded uncertain factors are taken into account, the local stiffness features can be embodied by interval processes rather than specific time histories ($u_i(t) \to u_i(\mathbf{x},\ t)$, $i = 1, 2, \cdots, NC$). Thereby, the deterministic optimization framework in Eq. (4) is actually infeasible due to the invalid constraints. In order to effectively realize the uncertainty-based stiffness limits, the following reliability-oriented optimization formulation is established and expressed as,

$$
\begin{aligned}
&\min_{\eta_e}\ M = \rho_0 \sum_{e=1}^{NE} \eta_e V_e \\
&\text{s.t.}\quad \mathbf{M}(\mathbf{x},\ \eta_e)\ddot{\mathbf{u}}(\mathbf{x},\ t) + \mathbf{C}(\mathbf{x},\ \eta_e,\ E_e)\dot{\mathbf{u}}(\mathbf{x},\ t) + \mathbf{K}(\mathbf{x},\ E_e)\mathbf{u}(\mathbf{x},\ t) = \mathbf{f}(\mathbf{x},\ t) \\
&\qquad R_s\left(\mathbf{x},\ u_i(t),\ T\right) = R_s\left(\mathbf{L}^T\mathbf{u}(\mathbf{x},\ t),\ T\right) \geq R_{cri} \\
&\qquad E_e = E_0\left(\alpha\eta_e^p + (1-\alpha)\eta_e\right)\Big|_{\mathbf{x}} \\
&\qquad \frac{\underline{\rho}}{\rho_0} \leq \eta_e \leq 1, \quad 0 \leq t \leq T \\
&\qquad e = 1, 2, \cdots, NE \\
&\qquad \mathbf{x} \in \mathbf{x}^{\mathbf{I}} = \left[\underline{\mathbf{x}},\ \overline{\mathbf{x}}\right] = \left[\mathbf{x_0} - \mathbf{x_r},\ \mathbf{x_0} + \mathbf{x_r}\right] = \mathbf{x_0} + \mathbf{x_r} \circ \boldsymbol{\zeta}
\end{aligned}
\tag{27}
$$

where $R_s\left(\mathbf{x},\ u_i(t),\ T\right)$ indicates the full life-cycle reliability index corresponding to the local stiffness behavior, and R_{cri} means the reliability threshold. Obviously, how to rationally define and further explicitly analyze the time-variant reliability index is the key to smoothly achieve the above DRBTO task. The following sections present the implementation details of this proposed DRBTO framework.

4.2 Non-probabilistic time-variant reliability (NTR) estimation for local stiffness safety

With regard to any topological structures, we are always interested in the comparison between the actual performance $u_i(\mathbf{x},\ t)$ and the given criteria value u_{cri} over its entire

service period $[0,\ T]$. Nevertheless, due to the multi-source uncertainties, the definite safety criterion $G_i(\mathbf{x},\ t)=u_{cri}-u_i(\mathbf{x},\ t)\geq 0$ may not be given and then the reliability judgment is very necessary. Different from the static reliability concepts, the NTR evaluation should consider not only the dynamic boundary rules of $\mathbf{L}^T\mathbf{u}(\mathbf{x},\ t)$, but also the changing time-dependency properties of $\rho_{u_i}(t_k,\ t_{k+1})$. In this study, inspired by the first-passage principle [48], the NTR judgement for measuring local stiffness safety of topological structures (existence of failure risk) is defined as,

$$\begin{aligned} R_s\left(\mathbf{x},\ u_i(t),\ T\right)&=\eta\left\{\forall t\in[0,\ T]:\ G_i(\mathbf{x},\ t)=u_{cri}-\left\|u_i(\mathbf{x},\ t)\right\|_\infty\geq 0\right\}\\ &\approx 1-\eta\left\{\left(G_i(\mathbf{x},\ 0)<0\right)\cup\left(N_{pass}(0,\ T)>0\right)\right\}\end{aligned},\quad 0\leq t\leq T \tag{28}$$

where $G_i(\mathbf{x},\ t)$ means the limit-state interval process relative to $u_i(\mathbf{x},\ t)$; $G_i(\mathbf{x},\ 0)<0$ indicates initial failure and $N_{pass}(0,\ T)$ is set as the out-crossing number during the whole time period; $\eta(\cdot)$ stands for the possibility of event occurrence. According to the above-mentioned time-discretization treatment, Eq. (28) can be further expressed by

$$R_s\left(\mathbf{x},\ u_i(t),\ T\right)=1-\min\left\{1,\ \left[\eta\left(G_i(\mathbf{x},\ 0)<0\right)+\left(\sum_{k=1}^{N_t}\phi_k\right)\Delta t\right]\right\} \tag{29}$$

where ϕ_k represents the out-crossing rate at instant time t_k that satisfies

$$\phi_k\Delta t=\eta\left\{G_i(\mathbf{x},\ t_{k-1})\geq 0\cap G_i(\mathbf{x},\ t_k)<0\right\}=\frac{A_k^{shaded}}{A_k^{total}} \tag{30}$$

where A_k^{shaded} and A_k^{total} are the interference and total feasible areas, respectively, as shown in Fig. 4. It should be emphasized that the mathematical expression for solution of ϕ_k relies not only on the relation between the envelope region of time-discretized interval variables $G_i(\mathbf{x},\ t_{k-1})$ and $G_i(\mathbf{x},\ t)$, but also on the geometric limits $G_i(\mathbf{x},\ t_{k-1})=0$ and $G_i(\mathbf{x},\ t_k)=0$. Specific theoretical contents have been expounded by our previous works in Refs. [36, 49].

By traversing all cases of changing counting index k, $R_s\left(\mathbf{x},\ u_i(t),\ T\right)$ will be recursively calculated for measuring the likelihood of safety/failure. However, there is an obvious shortcoming that the above-mentioned reliability measure cannot be used to describe the safety margin ($R_s\left(\mathbf{x},\ u_i(t),\ T\right)\equiv 1$), which will even bring adverse conditions of differential discontinuity for design sensitivities (may lead to iteration instability for layout updating). In order to avoid such undesirable scenario, another reliability definition based on the safety factor is proposed herein in the premise of absolutely safe conditions (as shown in

Fig. 5). That is,

$$R_s\left(\mathbf{x},\ u_i(t),\ T\right)=1+\min_{1\le k\le N_t}\left(-\xi_2-1\right)=1+\min_{1\le k\le N_t}\left(\frac{G_{i,0}(\mathbf{x},\ t_k)}{G_{i,r}(\mathbf{x},\ t_k)}-1\right) \tag{31}$$

As a consequence, the proposed NTR index is eventually formulated into a piecewise function format as the following,

$$R_s\left(\mathbf{x},\ u_i(t),\ T\right)=\begin{cases}1-\min\left\{1,\ \left[\eta\left(G_i(\mathbf{x},\ 0)<0\right)+\left(\sum_{k=1}^{N_t}\phi_k\right)\Delta t\right]\right\}, & \text{Possible failure}\\ 1+\min\limits_{1\le k\le N_t}\left(\dfrac{G_{i,0}(\mathbf{x},\ t_k)}{G_{i,r}(\mathbf{x},\ t_k)}-1\right), & \text{Abosulte safety}\end{cases} \tag{32}$$

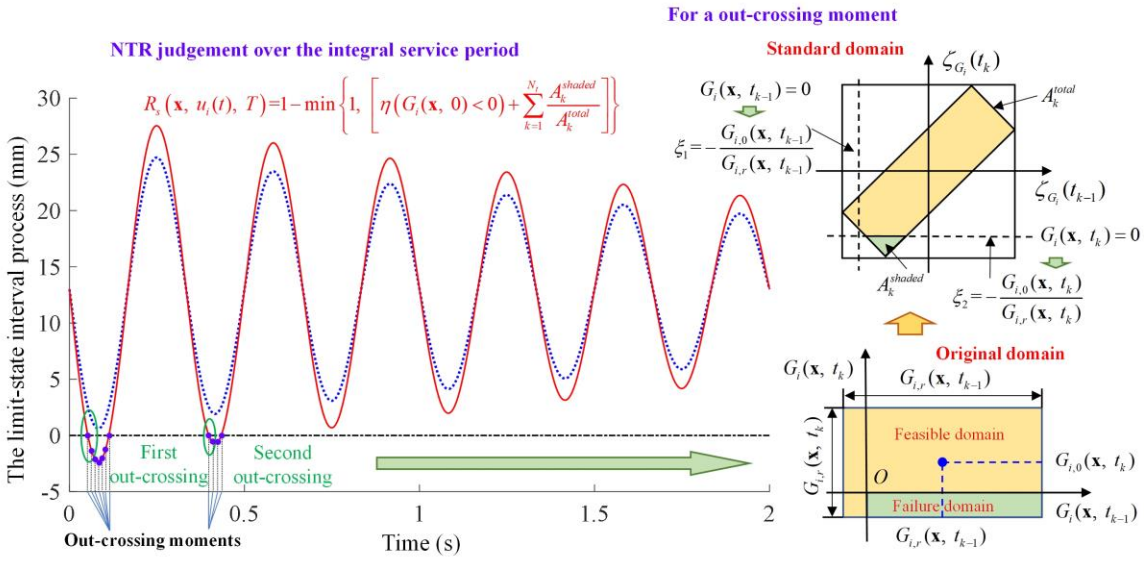

Fig. 4 Schematic diagram for calculating the reliability of out-crossing

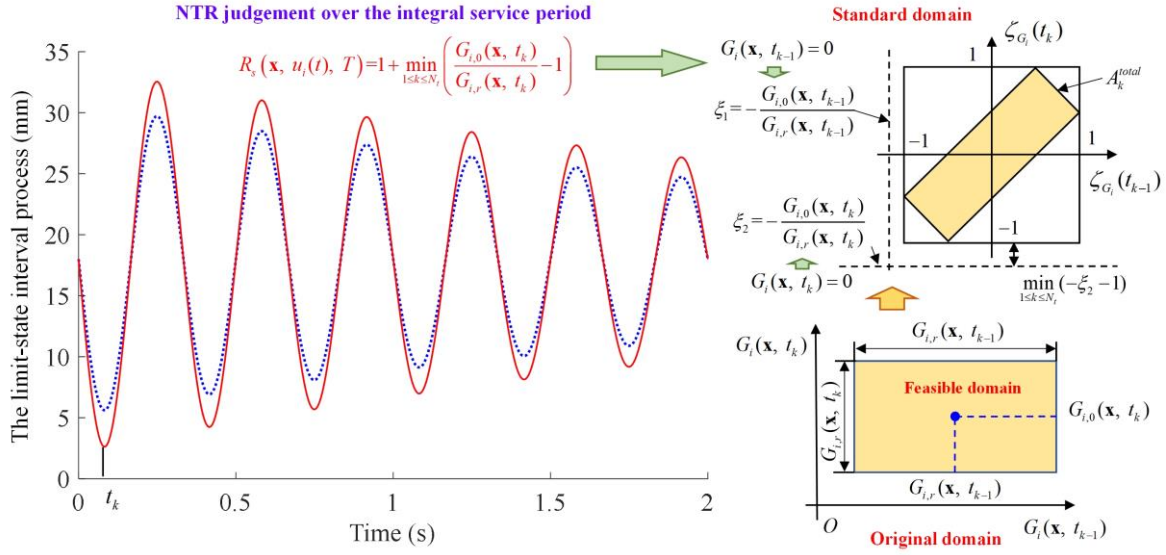

Fig. 5 Schematic diagram for calculating the reliability of absolutely safe conditions

In summary, the reliability-based performance constraints given in Eq. (27) are

analytically constructed, and additional auxiliary techniques for obtaining solution of the developed DRBTO scheme will be systematically explored in the next section.

5 Solution aspects

As we wish to apply a gradient-based optimization algorithm to find the optimal material distribution of the structure, it is necessary to evaluate the sensitivity of NTR index with respect to the design variables. Considering that the number of design variables is much larger than the number of constraints and objectives in TO, the adjoint variable method is preferred. Moreover, in view of the complexity of DRBTO model, auxiliary filtering technique is incorporated in this article as well.

5.1 Design sensitivity updating benchmarking to NTR constraints

According to the NTR definition in Eq. (32), the mathematical expression for $R_s\left(\mathbf{x},\ u_i(t),\ T\right)$ mainly relies on the performances of ϕ_k and $G_i(\mathbf{x},\ t_k)$, and the NTR measure is defined as a composite function of interval bounds of $u_i(\mathbf{x},\ t_{k-1})$ and $u_i(\mathbf{x},\ t_k)$. Thus, the reliability-oriented design sensitivity can be depicted as,

$$\begin{aligned}&\frac{\partial R_s\left(\mathbf{x},\ u_i(t),\ T\right)}{\partial \eta_e}=\sum_{k=1}^{N_t}\Theta(\phi_k,\ G_i(\mathbf{x},\ t_k))\\&=\sum_{k=1}^{N_t}\left(\kappa_1(t_{k-1})\frac{\partial \underline{u}_i(\mathbf{x},\ t_{k-1})}{\partial \eta_e}+\kappa_2(t_{k-1})\frac{\partial \overline{u}_i(\mathbf{x},\ t_{k-1})}{\partial \eta_e}+\kappa_3(t_k)\frac{\partial \underline{u}_i(\mathbf{x},\ t_k)}{\partial \eta_e}+\kappa_4(t_k)\frac{\partial \overline{u}_i(\mathbf{x},\ t_k)}{\partial \eta_e}\right)\end{aligned}\tag{33}$$

where the time-varying characteristics κ_i $(i=1,2,3,4)$ are known variables during the NTR solution procedure of the topological iteration, and other four partial derivative terms must be numerically analyzed. By introducing a Lagrangian multiplier vector $\boldsymbol{\lambda}(t)$, it results in,

$$\begin{aligned}&\frac{\partial u_i(\mathbf{x},\ t)}{\partial \eta_e}=\frac{\partial u_i(\mathbf{x},\ t)}{\partial \mathbf{u}(\mathbf{x},\ t)}\cdot\frac{\partial \mathbf{u}(\mathbf{x},\ t)}{\partial \eta_e}\\&+\boldsymbol{\lambda}^T(t)\frac{\partial}{\partial \eta_e}\left[\mathbf{M}(\mathbf{x},\ \eta_e)\ddot{\mathbf{u}}(\mathbf{x},\ t)+\mathbf{C}(\mathbf{x},\ \eta_e,\ E_e)\dot{\mathbf{u}}(\mathbf{x},\ t)+\mathbf{K}(\mathbf{x},\ E_e)\mathbf{u}(\mathbf{x},\ t)-\mathbf{f}(\mathbf{x},\ t)\right]\end{aligned}\tag{34}$$

Using the derivative expansion principle, Eq. (34) is further expressed as

$$\begin{aligned}&\frac{\partial u_i(\mathbf{x},\ t)}{\partial \eta_e}=\mathbf{L}^T\frac{\partial \mathbf{u}(\mathbf{x},\ t)}{\partial \eta_e}\\&+\boldsymbol{\lambda}^T(t)\left[\frac{\partial \mathbf{M}(\mathbf{x},\ \eta_e)}{\partial \eta_e}\ddot{\mathbf{u}}(\mathbf{x},\ t)+\frac{\partial \mathbf{C}(\mathbf{x},\ \eta_e,\ E_e)}{\partial \eta_e}\dot{\mathbf{u}}(\mathbf{x},\ t)+\frac{\partial \mathbf{K}(\mathbf{x},\ E_e)}{\partial \eta_e}\mathbf{u}(\mathbf{x},\ t)\right]\\&+\boldsymbol{\lambda}^T(t)\left[\mathbf{M}(\mathbf{x},\ \eta_e)\frac{\partial \ddot{\mathbf{u}}(\mathbf{x},\ t)}{\partial \eta_e}+\mathbf{C}(\mathbf{x},\ \eta_e,\ E_e)\frac{\partial \dot{\mathbf{u}}(\mathbf{x},\ t)}{\partial \eta_e}+\mathbf{K}(\mathbf{x},\ E_e)\frac{\partial \mathbf{u}(\mathbf{x},\ t)}{\partial \eta_e}\right]\end{aligned}\tag{35}$$

Twice derivative operations are rearranged as

$$\begin{aligned}\frac{\partial u_i(\mathbf{x},\ t)}{\partial \eta_e} &= \boldsymbol{\lambda}^T(t)\left[\frac{\partial \mathbf{M}(\mathbf{x},\ \eta_e)}{\partial \eta_e}\ddot{\mathbf{u}}(\mathbf{x},\ t)+\frac{\partial \mathbf{C}(\mathbf{x},\ \eta_e,\ E_e)}{\partial \eta_e}\dot{\mathbf{u}}(\mathbf{x},\ t)+\frac{\partial \mathbf{K}(\mathbf{x},\ E_e)}{\partial \eta_e}\mathbf{u}(\mathbf{x},\ t)\right]\\ &+\left(\frac{\partial \mathbf{u}(\mathbf{x},\ t)}{\partial \eta_e}\right)^T\left[\mathbf{M}(\mathbf{x},\ \eta_e)\ddot{\boldsymbol{\lambda}}(t)-\mathbf{C}(\mathbf{x},\ \eta_e,\ E_e)\dot{\boldsymbol{\lambda}}(t)+\mathbf{K}(\mathbf{x},\ E_e)\boldsymbol{\lambda}(t)+\mathbf{L}\right]\\ &+\left(\frac{\partial \mathbf{u}(\mathbf{x},\ t)}{\partial \eta_e}\right)^T\left[-\mathbf{M}(\mathbf{x},\ \eta_e)\dot{\boldsymbol{\lambda}}(t)+\mathbf{C}(\mathbf{x},\ \eta_e,\ E_e)\boldsymbol{\lambda}(t)\right]+\left(\frac{\partial \dot{\mathbf{u}}(\mathbf{x},\ t)}{\partial \eta_e}\right)^T\mathbf{M}(\mathbf{x},\ \eta_e)\boldsymbol{\lambda}(t)\end{aligned} \tag{36}$$

It indicates that since Eq. (36) holds for arbitrary $\boldsymbol{\lambda}(t)$, it may be simplified to choose a good multiplier that satisfies

$$\begin{cases}\mathbf{M}(\mathbf{x},\ \eta_e)\ddot{\boldsymbol{\lambda}}(t)-\mathbf{C}(\mathbf{x},\ \eta_e,\ E_e)\dot{\boldsymbol{\lambda}}(t)+\mathbf{K}(\mathbf{x},\ E_e)\boldsymbol{\lambda}(t)=-\mathbf{L}\\ \boldsymbol{\lambda}(t_s)=0,\ \dot{\boldsymbol{\lambda}}(t_s)=0,\ t\in[0,\ t_s]\end{cases} \tag{37}$$

where t_s corresponds to any instant time, for instance t_{k-1} or t_k. Note, such above adjoint formulation is analogous with the dynamic equilibrium equation, except of the terminal conditions. If applying a simple substitution operation $\boldsymbol{\Xi}(t_{ss})=\boldsymbol{\lambda}(t_s-t_{ss})$, Eq. (37) becomes

$$\begin{cases}\mathbf{M}(\mathbf{x},\ \eta_e)\ddot{\boldsymbol{\Xi}}(t_{ss})+\mathbf{C}(\mathbf{x},\ \eta_e,\ E_e)\dot{\boldsymbol{\Xi}}(t_{ss})+\mathbf{K}(\mathbf{x},\ E_e)\boldsymbol{\Xi}(t_{ss})=-\mathbf{L}\\ \boldsymbol{\Xi}(0)=0,\ \dot{\boldsymbol{\Xi}}(0)=0,\ t_{ss}\in[0,\ t_s]\end{cases} \tag{38}$$

As referred to Eqs. (24)-(25), boundary rules for determining $u_i(\mathbf{x},\ t_s)$ can be applied in advance. Hence, substitution of $\tilde{\mathbf{x}}_{\mathbf{min}}\big|_{t_s}$ and $\tilde{\mathbf{x}}_{\mathbf{max}}\big|_{t_s}$ into the defined adjoint equation leads one to obtain $\boldsymbol{\lambda}_{\mathbf{min}}(t)$ and $\boldsymbol{\lambda}_{\mathbf{max}}(t)$, respectively, using the classical Newmark difference scheme, and the partial derivatives are finally obtained and given by,

$$\begin{aligned}\frac{\partial \underline{u}_i(\mathbf{x},\ t_s)}{\partial \eta_e} &= \frac{\partial u_i(\tilde{\mathbf{x}}_{\mathbf{min}},\ t_s)}{\partial \eta_e}=\left(\boldsymbol{\lambda}_{\mathbf{min}}(t)\right)^T\\ &\cdot\left[\frac{\partial \mathbf{M}(\tilde{\mathbf{x}}_{\mathbf{min}},\ \eta_e)}{\partial \eta_e}\ddot{\mathbf{u}}(\tilde{\mathbf{x}}_{\mathbf{min}},\ t)+\frac{\partial \mathbf{C}(\tilde{\mathbf{x}}_{\mathbf{min}},\ \eta_e,\ E_e)}{\partial \eta_e}\dot{\mathbf{u}}(\tilde{\mathbf{x}}_{\mathbf{min}},\ t)+\frac{\partial \mathbf{K}(\tilde{\mathbf{x}}_{\mathbf{min}},\ E_e)}{\partial \eta_e}\mathbf{u}(\tilde{\mathbf{x}}_{\mathbf{min}},\ t)\right]\end{aligned} \tag{39}$$

and

$$\begin{aligned}\frac{\partial \bar{u}_i(\mathbf{x},\ t_s)}{\partial \eta_e} &= \frac{\partial u_i(\tilde{\mathbf{x}}_{\mathbf{max}},\ t_s)}{\partial \eta_e}=\left(\boldsymbol{\lambda}_{\mathbf{max}}(t)\right)^T\\ &\cdot\left[\frac{\partial \mathbf{M}(\tilde{\mathbf{x}}_{\mathbf{max}},\ \eta_e)}{\partial \eta_e}\ddot{\mathbf{u}}(\tilde{\mathbf{x}}_{\mathbf{max}},\ t)+\frac{\partial \mathbf{C}(\tilde{\mathbf{x}}_{\mathbf{max}},\ \eta_e,\ E_e)}{\partial \eta_e}\dot{\mathbf{u}}(\tilde{\mathbf{x}}_{\mathbf{max}},\ t)+\frac{\partial \mathbf{K}(\tilde{\mathbf{x}}_{\mathbf{max}},\ E_e)}{\partial \eta_e}\mathbf{u}(\tilde{\mathbf{x}}_{\mathbf{max}},\ t)\right]\end{aligned} \tag{40}$$

where the Rayleigh damping $\mathbf{C}(\tilde{\mathbf{x}}_{\mathbf{max}},\ \eta_e,\ E_e)=\alpha_r\mathbf{M}(\tilde{\mathbf{x}}_{\mathbf{max}},\ \eta_e)+\beta_r\mathbf{K}(\tilde{\mathbf{x}}_{\mathbf{max}},\ E_e)$ is assumed and the coefficients α_r and β_r are regarded as design-independent; the differential terms corresponding to topological constitutive matrices can be given by

$$\frac{\partial \mathbf{M}(\tilde{\mathbf{x}}_{\max},\ \eta_e)}{\partial \eta_e} = \mathbf{M}_{\mathbf{e}}^{*}(\tilde{\mathbf{x}}_{\max}),\qquad \frac{\partial \mathbf{K}(\tilde{\mathbf{x}}_{\max},\ E_e)}{\partial \eta_e} = \left(\alpha p \eta_e^{p-1} + (1-\alpha)\right)\mathbf{K}_{\mathbf{e}}^{*}(\tilde{\mathbf{x}}_{\max}) \tag{41}$$

and

$$\frac{\partial \mathbf{C}(\tilde{\mathbf{x}}_{\max},\ \eta_e,\ E_e)}{\partial \eta_e} = \alpha_r \mathbf{M}_{\mathbf{e}}^{*}(\tilde{\mathbf{x}}_{\max}) + \beta_r \left(\alpha p \eta_e^{p-1} + (1-\alpha)\right)\mathbf{K}_{\mathbf{e}}^{*}(\tilde{\mathbf{x}}_{\max}) \tag{42}$$

in which $\mathbf{M}_{\mathbf{e}}^{*}$ and $\mathbf{K}_{\mathbf{e}}^{*}$ represent mass and stiffness matrices of the e-th element filled with solid materials, respectively.

To sum up, the design sensitivity of $R_s\left(\mathbf{x},\ u_i(t),\ T\right)$ with respect to η_e are calculated from Eqs. (33)-(42). Certainly, compared with the deterministic topology design procedure, the proposed uncertainty-oriented optimization framework needs much larger computational costs, especially for obtaining the solution as presented in this section. Therefore, with respect to complicated engineering problems, high-performance parallel computing services are commonly necessary.

5.2 Density filtering and smoothing treatments

To eliminate the checkerboard problem as well as the mesh-dependency shortage od the DRBTO model, some restrictions are imposed on the design policy. Herein, the well-known sensitivity-filtering technique is applied, whose transformation scheme can be expressed as

$$\frac{\partial R_s\left(\mathbf{x},\ u_i(t),\ T\right)}{\partial \eta_e} = \frac{\sum_{s=1}^{NE}\left(\eta_e D_{es}\dfrac{\partial R_s\left(\mathbf{x},\ u_i(t),\ T\right)}{\partial \eta_e}\right)}{\eta_e \sum_{s=1}^{NE} D_{es}},\ e=1,2,...NE,\ i=1,2,...NC \tag{43}$$

where the nonnegative weight factor D_{es} is deduced by

$$D_{es} = r_f - Dis(e,s) \qquad \text{in which} \qquad \left\{ s \middle| Dis(e,\ s) \le r_f,\ s=1,2,...,NE \right\} \tag{44}$$

$Dis(e,s)$ denotes the center-to-center distance between two elements e and s; r_f denotes the filter radius, which is set as 1.5-2 times of the element size. Note that D_{es} is zero outside the filter area, and it can be decay linearly versus the distance $Dis(e,s)$.

Therefore, instead of using the sensitivity solutions given by Eq. (33), the modified filtering results are fed to the optimizer. Apparently, $\dfrac{\partial R_s\left(\mathbf{x},\ u_i(t),\ T\right)}{\partial \eta_e}$ can also degenerate to the original $\dfrac{\partial R_s\left(\mathbf{x},\ u_i(t),\ T\right)}{\partial \eta_e}$ if r_f is valued as zero; On the contrast, all the sensitivities in the design domain will be identical if r_f is close to infinity.

5.3 Concrete implement process of the proposed optimization scheme

To clearly manifest the overall iterative process of the proposed DRBTO framework in this work, the operation procedures are successively summarized in Fig. 6 and Table 1, which are categorized into three parts of preparatory work, NTR judgement and DRBTO solution. Particularly, the novelty in the analysis phase (N1. Interval-process representation; N2. NTR assessment via first-passage model) and the modeling phase (N3. The DRBTO framework; N4. NTR-based sensitivity updating) are highlighted in Fig. 6. The following gives the implementation details of this DRBTO framework.

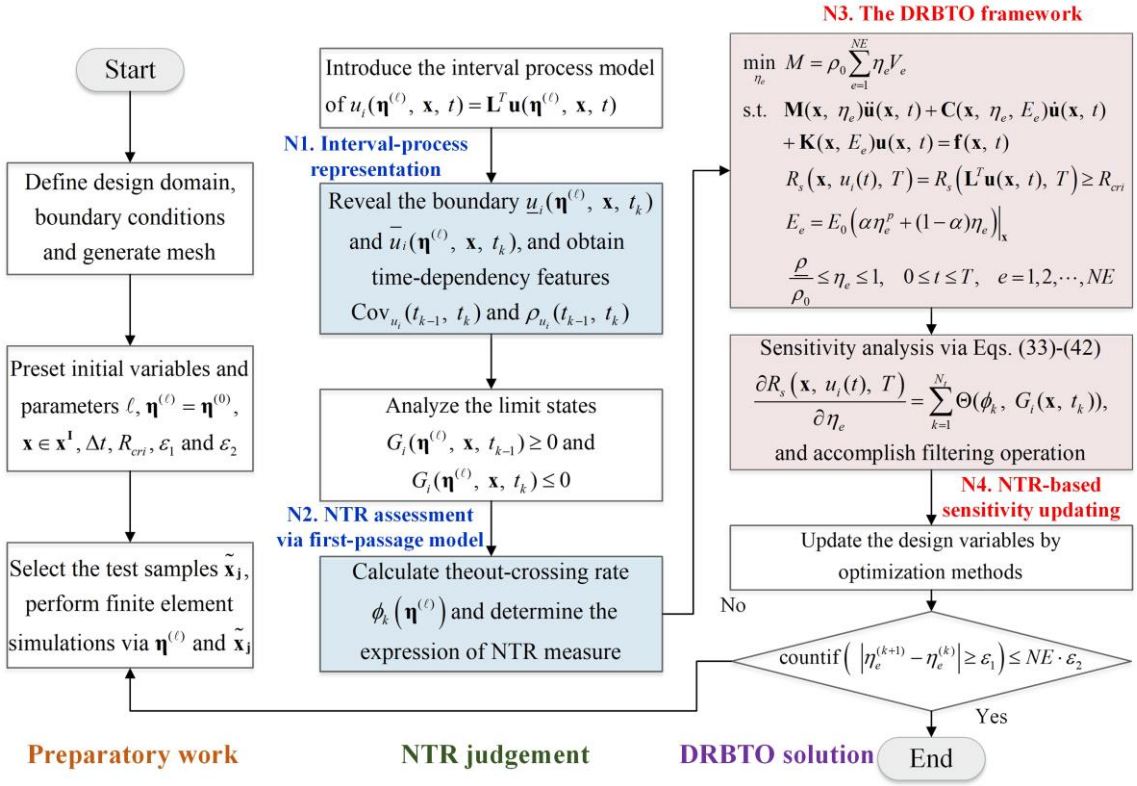

Fig. 6 Flowchart of the procedure for accomplishment of the presented DRBTO scheme

Step 1. Preset initial design variables and computational parameters: the cycle number ℓ; design variables $\boldsymbol{\eta}^{(\ell)}=\boldsymbol{\eta}^{(0)}=\left(\eta_e^{(0)}\right)$, $e=1,2,...,NE$; static uncertainty inputs $\mathbf{x}\in\mathbf{x}^{\mathbf{I}}=\mathbf{x}_{\mathbf{0}}+\mathbf{x}_{\mathbf{r}}\circ\boldsymbol{\zeta}$; the time increment Δt; the reliability threshold R_{cri} and small convergence numbers ε_1 and ε_2.

Step 2. Select the test samples $\tilde{\mathbf{x}}_{\mathbf{j}}$ ($j=1,2,...,l$) for all interval parameters, and perform a certain number of dynamic FEM simulations via $\boldsymbol{\eta}^{(\ell)}$ and $\tilde{\mathbf{x}}_{\mathbf{j}}$ using classical Newmark difference method.

Step 3. Introduce the interval process model to quantify local stiffness responses $u_i(\boldsymbol{\eta}^{(\ell)},\ \mathbf{x},\ t)=\mathbf{L}^T\mathbf{u}(\boldsymbol{\eta}^{(\ell)},\ \mathbf{x},\ t)$, $i=1,2,...,NC$. Then, combine with the time-discretization

principle ($t_k = k\Delta t$) and interval-process collocation theorem to reveal boundary rules of concerned nodal displacement $\underline{u}_i(\boldsymbol{\eta}^{(\ell)}, \mathbf{x}, t_k)$ and $\overline{u}_i(\boldsymbol{\eta}^{(\ell)}, \mathbf{x}, t_k)$ as referred by Eqs. (14) -(25). Furthermore, the time-dependent features $\mathrm{Cov}_{u_i}(t_{k-1}, t_k)$ and $\rho_{u_i}(t_{k-1}, t_k)$ are obtained through the first-order perturbation approach.

Table 1 The pseudo-code of the proposed method

Input: The meshed model, initial design variables $\boldsymbol{\eta}^{(0)}$, static uncertainty inputs $\mathbf{x}^{\mathbf{I}}$, the time increment Δt, the convergence tolerance ε_1 and ε_2

Output: The final optimal configuration

1: **While** $N_{ch} \le NE \cdot \varepsilon_2$, **Step** 1, **do**

2: Generate quadrature nodes $\tilde{\upsilon}_{j,s}$ and perform dynamic FEM simulations via $\boldsymbol{\eta}^{(\ell)}$ and $\tilde{\mathbf{x}}_{\mathbf{j}}$.

3: Obtain the boundaries of local responses $u_i(\boldsymbol{\eta}^{(\ell)}, \mathbf{x}, t)$ through interval-process collocation theorem:

$$u_i(\mathbf{x}_{\mathbf{j}}, t_k) \leftarrow \frac{1}{Nq}\sum_{s=1}^{Nq} u_i(\tilde{\mathbf{x}}_{\mathbf{j},\mathbf{s}}, t_k) + \frac{2}{Nq}\sum_{m=1}^{r}\sum_{s=1}^{Nq} u_i(\tilde{\mathbf{x}}_{\mathbf{j},\mathbf{s}}, t_k) C_m(\tilde{\upsilon}_{j,s}) C_m(\upsilon_j)$$

4: Calculate the time-dependency features $\mathrm{Cov}_{u_i}(t_{k-1}, t_k)$ and $\rho_{u_i}(t_{k-1}, t_k)$

$$\rho_{u_i}(t_{k-1}, t_k) \leftarrow \frac{\sum_{j=1}^{l}\left[\frac{\partial u_i(\mathbf{x}_{\mathbf{0}}, t_{k-1})}{\partial x_{j,0}(t_{k-1})} \cdot \frac{\partial u_i(\mathbf{x}_{\mathbf{0}}, t_k)}{\partial x_{j,0}(\mathbf{x}_{\mathbf{0}}, t_k)} \cdot x_{j,r}(t_{k-1}) \cdot x_{j,r}(t_k) \cdot \rho_{x_j}(t_{k-1}, t_k)\right]}{\sqrt{\sum_{j=1}^{l}\left[\left(\frac{\partial u_i(\mathbf{x}_{\mathbf{0}}, t_{k-1})}{\partial x_{j,0}} \cdot x_{j,r}\right)^2\right]} \cdot \sqrt{\sum_{j=1}^{l}\left[\left(\frac{\partial u_i(\mathbf{x}_{\mathbf{0}}, t_k)}{\partial x_{j,0}} \cdot x_{j,r}\right)^2\right]}}, \rho_{u_i}(t_1, t_2) \leftarrow \left.\frac{\mathrm{Cov}_{u_i}(t_1, t_2)}{\sqrt{D_{u_i}(t_1)} \cdot \sqrt{D_{u_i}(t_2)}}\right|_{\mathbf{x}}$$

5: Judge the limit states, determine the expression of NTR measure and calculate $R_s(\mathbf{x}, u_i(t), T)$

$$R_s(\mathbf{x}, u_i(t), T) \leftarrow \eta\left\{\forall t \in [0, T]: G_i(\mathbf{x}, t) = u_{cri} - \|u_i(\mathbf{x}, t)\|_\infty \ge 0\right\}$$

6: Establish the DRBTO model as Eq. (27)

7: Carry out the sensitivity analysis and filtering operation of NTR measure:

$$\frac{\partial R_s(\mathbf{x}, u_i(t), T)}{\partial \eta_e} \leftarrow \sum_{k=1}^{N_t}\left(\kappa_1(t_{k-1})\frac{\partial \underline{u}_i(\mathbf{x}, t_{k-1})}{\partial \eta_e} + \kappa_2(t_{k-1})\frac{\partial \overline{u}_i(\mathbf{x}, t_{k-1})}{\partial \eta_e} + \kappa_3(t_k)\frac{\partial \underline{u}_i(\mathbf{x}, t_k)}{\partial \eta_e} + \kappa_4(t_k)\frac{\partial \overline{u}_i(\mathbf{x}, t_k)}{\partial \eta_e}\right)$$

8: Utilize the MMA algorithm to update the design variables $\boldsymbol{\eta}^{(\ell+1)}$

9: Calculate the relative change amount of immediate density:

$$N_{ch} \leftarrow \mathrm{countif}\left(\left|\eta_e^{(k+1)} - \eta_e^{(k)}\right| \ge \varepsilon_1\right)$$

10: **End While**

11: **Print the optimization layout**

Step 4. Analyze the limit states $G_i(\boldsymbol{\eta}^{(\ell)}, \mathbf{x}, t_{k-1}) \ge 0$ and $G_i(\boldsymbol{\eta}^{(\ell)}, \mathbf{x}, t_k) \le 0$ to calculate the out-crossing rate $\phi_k\left(\boldsymbol{\eta}^{(\ell)}\right)$, and further determine the mathematical expression of NTR measure after the superposition calculation. In addition, accomplish the design

sensitivity analysis and filtering operation for acquisition of $\frac{\partial R_s\left(\mathbf{x},\ u_i\left(\boldsymbol{\eta}^{(\ell)},\ t\right),\ T\right)}{\partial \eta_e}$ based on the dynamic adjoint equation and density interpolation equation, as stated in Section 5.1.

Step 5. Invoke the sensitivity-driven design framework based on the proposed DRBTO model as summarized in Eq. (27). If $\ell = 0$, sequential operations are needed and go to Step 6. If the convergence criterion is satisfied, the TO process terminates; otherwise, go to step 6 for the next cycle. Note, the convergence condition is defined as

$$N_{ch}=\text{countif}\left(\ \left|\eta_e^{(k+1)}-\eta_e^{(k)}\right|\geq \varepsilon_1\right)\leq NE\cdot\varepsilon_2 \tag{45}$$

Step 6. Update the design variables by virtue of the gradient information $\frac{\partial R_s\left(\mathbf{x},\ u_i\left(\boldsymbol{\eta}^{(\ell)},\ t\right),\ T\right)}{\partial \eta_e}$; then, reset $\ell = \ell+1$, and return to Step 2.

Step 7. Validate all analysis and design results obtained using the developed DRBTO model.

5.4 Discussions on solution details

In this part, additional clarifications are provided in the following to further explain the obtained solutions.

A. Material interpolation model

For the frequency-domain responses or time-domain responses of topological structure concerning in DTO, the element stiffness is weakened due to the material removal and then the localized deformation caused by inertial load and gravity force may occur in the structural impaired region. For a typical standard SIMP model $E_e=\eta_e^p E_0$, the intermediate density $\eta_e\in(0,1)$ is penalized and then gathers to both ends of 0 or 1. However, a significant difference may be generated between the stiffness and the mass of each element, particularly when the pseudo-density is small. This also can be clearly characterized by the curve of ρ_e/E_e in Fig. 7 (a). This ratio varies toward zero infinitely large when η_e tends to 0. Hence, a reasonable interpolation model between elastic modulus and material density should be established to overcome the incompatibility of stiffness and mass in Fig. 7 (a). Inspired by improved models proposed by Pedersen [50], Bruyneel and Duysinx [51], Eq. (3) created by Zhu [52] utilizes a linear adjustable parameter α and nonlinear penalty factor p for material interpolation. The curves of the polynomial interpolation model in terms of penalization function P and mass-stiffness ratio ρ_e/E_e with α=15/16 and $p=3$ are

plotted in Fig. 7 (b). It can be concluded that this model not only retains the advantages of the standard SIMP model transforming the discrete optimization to continuous optimization, but also solves the problem of mass/stiffness mismatch and localized deformation when the pseudo-density approaches zero.

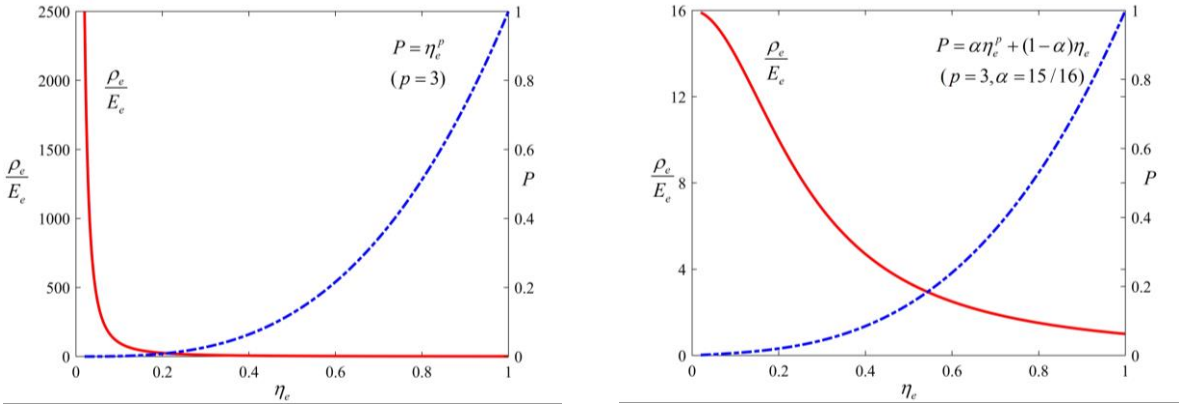

(a) the standard SIMP model (b) the polynomial interpolation model

Fig. 7 Comparation of two interpolation models

B. The time increment Δt

Apparently, the $\rho_{x_j}(t_{k-1},\ t_k)$ is directly related to $u_i(\mathbf{x_0},\ t_{k-1})$ and $u_i(\mathbf{x_0},\ t_k)$, and then to the time increment Δt. For constructing an effective uncertainty-oriented DRTO model, Δt should be selected properly for specific situations to balance the accuracy and efficiency of transient dynamic analysis, auto-correlation coefficient calculation and safety assessment. As revealed in Ref. [53], the criteria $\left\{\Delta t \mid \rho_{u_i}(t_{k-1},\ t_k)\geq 0.9\right\}$ should be satisfied in general to avoid missing the failure event $\left\{G_i(\mathbf{x},\ t_{k-1})\geq 0 \cap G_i(\mathbf{x},\ t_k)<0\right\}$. Furthermore, the repeated tests and modeling updating strategies may also be applied for addressing the issues that the $\rho_{x_j}(t_{k-1},\ t_k)$ is sensitive to Δt or the precision requirements are very high. On one hand, the dichotomy verification can be used to get the inflection point of Δt by segmenting it continuously until the $\rho_{x_j}(t_{k-1},\ t_k)$ of two segmentations before and after reaches the preset convergence condition; on the other hand, an adaptive sampling strategy in the design of the experiment (DOE) framework may be adopted to build the surrogate model between $\rho_{x_j}(t_{k-1},\ t_k)$ and Δt, and then could be used to determine its final value.

C. Truncated order of Chebyshev orthogonal polynomial

It is undeniable that the analysis error of responses interval largely depends on the truncated order of the Chebyshev series. The complicated mapping relation between static uncertain inputs and dynamic displacement responses can be obtained by high-order Chebyshev polynomial. Nonetheless, applying too high order of polynomials will increase

the computational cost, significantly. The precision of polynomial approximation may converge when the truncated order r increases to a certain degree. r is a recommended odd number chosen from 3 to 11 according to engineer applications [15].

Additionally, the order r also determines the error of polynomial coefficients obtained from Eq. (19). Based on the Gauss-Chebyshev quadrature formula [47], the truncation error of $a_{m,i}(t_k)$ is given by

$$R = \frac{f^{(2q)}(\upsilon_j)}{(2Nq)!}\int_{-1}^{1}\frac{L_q^2(x)}{\sqrt{1-x^2}}dx = \frac{2\pi}{2^{2Nq}(2Nq)!}f^{2Nq}(\upsilon_j) \tag{46}$$

For the r-order Chebyshev orthogonal polynomial, $Nq \geq (r+1)/2$ (r is an odd number) or $Nq \geq (r+2)/2$ (r is an even number) may make the error R equal to 0 in view of the derivation principle. Thus, more quadrature nodes are needed to ensure a high precision of the coefficient solution. Nq is set as not less than 6 in general engineering applications to balance both computational efficiency and precision.

D. Comparations of NTR index based on different out-crossing rate

Obviously, the first-passage model based on the out-crossing rate is the precondition for the NTR assessment of local stiffness. It was first proposed by Rice [54] in the framework of probability theory and then has been intensively investigated by many scholars. For over several decades, the PHI2 method developed by Andrieu-Renaud et al. [55] is one of the most mainstream methods, which can transform the NTR issues into static reliability of the parallel system to improve the accuracy and efficiency. The main formula may be summarized as

$$\phi_k \Delta t \approx \Pr\left\{G_i(\mathbf{x},\ t_{k-1}) \geq 0 \cap G_i(\mathbf{x},\ t_k) < 0\right\} \approx \Phi_2\left(\beta(t_{k-1}), -\beta(t_k), \rho_{G_i}(t_{k-1}, t_k)\right) \tag{47}$$

where $\Pr\{*\}$ is the probability of event occurrence; Φ_2 denotes the binomial cumulative distribution function; $\beta(t_{k-1})$ and $\beta(t_k)$ stand for the reliability index of instant time t_{k-1} and t_k and $\rho_{G_i}(t_{k-1}, t_k)$ signifies the correlation coefficient between the two events $G_i(\mathbf{x},\ t_{k-1}) \geq 0$ and $G_i(\mathbf{x},\ t_k) < 0$. In general, the Poisson model is utilized to calculate the cumulative failure probability, and the probability of i-times out-crossing within the service period $[0,\ T]$ may be expressed as

$$\Pr\left\{N_{pass}(0,\ T) = i\right\} = \frac{1}{i!}\left[\int_0^T \phi(t)dt\right]^i \exp\left[-\int_0^T \phi(t)dt\right] \tag{48}$$

Then, the NTR index may be obtained by assigning $i = 0$. When the initial failure $P_f(0)$ is

considered, the NTR is rewritten as

$$R_s\left(\mathbf{x},\ u_i(t),\ T\right)=\Pr\left\{N_{pass}(0,\ T)=0\right\}=P_f(0)\exp\left[-\int_0^T\phi(t)dt\right] \tag{49}$$

However, the above equations depend on accurate probability distribution of structural parameters. In fact, the interval bounds of uncertain parameters are easier to obtain as mentioned in Section 3.1. To this end, Jiang et al. [56] proposed a hybrid reliability approach based on probability and interval uncertainties for the problems with limited information. The out-crossing rate $\phi(t)$ is no longer a fixed value in this method, but an interval $\left[\underline{\phi}(t),\overline{\phi}(t)\right]$ is involved. Then, the NTR index is calculated by

$$\underline{R}_s\left(\mathbf{x},\ u_i(t),\ T\right)=\underline{P}_f(0)\exp\left[-\int_0^T\underline{\phi}(t)dt\right]\ \text{ and }\ \overline{R}_s\left(\mathbf{x},\ u_i(t),\ T\right)=\overline{P}_f(0)\exp\left[-\int_0^T\overline{\phi}(t)dt\right] \tag{50}$$

To summarize, this remains an open question to define out-crossing rates and NTR indices based on different hypotheses and uncertainty quantitative models. Introducing them into the DRBTO model, the final topological configuration will disagree with each other due to various NTR constraints. Notably, the NTR measurement in our work has a wide prospect in engineering applications owing to its simplicity and convenience.

6 Numerical examples

In order to clarify the feasibility of the developed DRBTO framework in this work, 3 numerical examples are investigated in this section. In the first example, a rectangular plate structure is used as the basis to illustrate the effects of NTR measures. In the second example, the DRBTO is carried out with different uncertainty inputs. Eventually, a more complicated wing rib structure is studied for the comparison between static TO and dynamic TO strategies. In terms of material property dispersion, varying environmental conditions and dynamic load processes, Young's modulus, damping coefficient and external loads are considered as uncertainties, whose fluctuating levels are set to be no more than 25% according to engineering practice. In practice, the interval boundaries should be determined after a series of quantification operations of sample data for specific problems. In addition, for all examples, the material of the initial design is uniformly distributed with pseudo-density $\boldsymbol{\eta}^{(0)}=\left(\eta_e^{(0)}\right)=1,\ e=1,2,...,NE$. The parameters regarding the polynomial interpolation model are set as $p=3$ and $\alpha=15/16$. The filter radius is set as 1.5 times the element size. The classical method of moving asymptotes (MMA) is utilized to perform the gradient-based optimization.

6.1 Optimization for a rectangular plate structure

As shown in Fig. 8 (a), the design domain is a $120\ \text{mm}\times 40\ \text{mm}$ rectangular plate with a thickness of $1\ \text{mm}$ and it is uniformly discretized by plane four-node elements with $1\ \text{mm}$ size. The left of the upper edge is fixed and two dynamic loads are vertically applied at the lower-right corner (F_1) and the upper-right corner (F_2), respectively. The time step is taken as Δt=0.004 s for dynamic FEM simulations duration, which is $T=0.4\ \text{s}$. Regardless of the uncertainties of initial property parameters, it is assumed that Young's modulus $E_0=210\ \text{GPa}$, structural density $\rho_0=7800\ \text{kg/m}^3$ and Poisson's ratio μ=0.3 for fully solid material. The coefficients for the Rayleigh damping are chosen as $\alpha=0$ and β=0.02. To demonstrate the effectiveness of the proposed DRBTO, the DRTO framework under deterministic conditions as presented in Section 2 is also applied, in which the deterministic loads (F_1^c and F_2^c) denoted by the center lines in Fig. 8 (b) are employed. When the DRBTO strategy is applied, the uncertain characteristics are computed and listed in Table 2. The changing of load deviation with time is plotted in Fig. 8 (b). To demonstrate the superiority of the NTR index, an uncertainty-oriented DRTO scheme (UDRTO) considering the time-point reliability of maximum displacement is further developed.

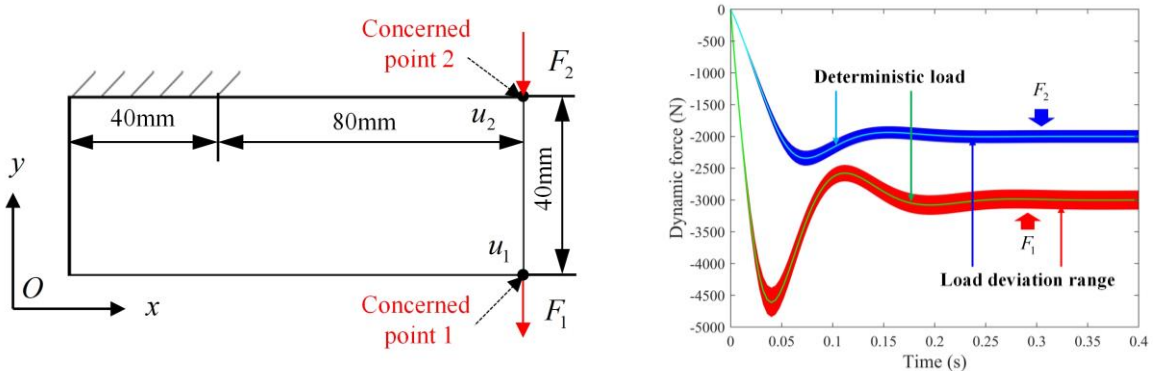

(a) The rectangular plate structure (b) The time-variant load

Fig. 8 Design domain and boundary conditions

Table 2 Uncertain characteristics of the rectangular plate structure

Parameters	E^I (GPa)	β^I	F_1^I (N)	F_2^I (N)
Values	$[199.5, 220.5]$	$[0.018, 0.022]$	$[0.95F_1^c, 1.05F_1^c]$	$[0.95F_2^c, 1.05F_2^c]$
Fluctuating level	10%	20%	10%	10%

Moreover, the displacements at the loading points 1 and 2 along y direction are regarded as the concerned local stiffness responses. Their allowable displacements are set as $-5.5\ \text{mm}$ and $-4.5\ \text{mm}$ for DRTO, DRBTO, and UDRTO strategies, and different reliability thresholds with R_{cri}=0.95 and R_{cri}=0.999 are adopted for both u_1 and u_2. The

indicator of relative mass fraction (*RMF*) is used to replace the objective function in terms of mass M. The iterative curve of *RMF* and the configuration change within 150 steps under different optimization strategies are plotted in Fig. 9, the cloud atlas for the displacements along the y direction with deterministic parameters (named as nominal displacement) at 0.4s are plotted in Fig. 10, the *RMF* and NTR of the final topological structures are summarized in Table 3, and the dynamic displacement, velocity and acceleration responses of points 1 and 2 along the y direction considering multi-source uncertainties are summarized in Table 4. For the convergence criterion, the tolerance ε_1 is generally assigned as 10^{-3} [57]. In addition, the influence of the small number ε_2 on final optimal configurations is investigated and the obtained results are presented in Table 5. From the obtained numerical results, one can conclude that:

1. All DRTO, DTBTO and UDRTO processes are shown well convergence and stability. The final topological structures are black-and-white designs with clear layouts. Only a few intermediate densities appear at the boundary areas, which may be attributed to the smoothing treatments of density filtering.

2. As listed in Table 3, the configurations obtained by the DRBTO and UDRTO strategies have greater *RMF* compared with that obtained by the DRTO strategy. Thicker components or additional members will be generated to resist the displacement fluctuation caused by multi-source uncertainties. This phenomenon becomes more obvious with the increase of the reliability threshold. Moreover, the responses from the DRTO are larger than those from other strategies. Taking displacement responses as an example, their lower bounds from DRTO far exceed the allowable displacements, while their lower bounds from DRBTO and UDRTO only slightly exceed them at a few discrete moments, which are marked by circle at their nominal displacements in Table 4. Thus, the design results based on DRTO are not applicable once uncertain factors are considered.

3. In some cases, the optimization results are different under time-variant reliability and time-point reliability criterions. For R_{cri}=0.95, the topological result based on time-point reliability is more conservative (*RMF*: 45.2% for DRBTO and 46.0% for UDRTO), because it only focuses on the displacement response at the most dangerous time and does not consider the displacement crossing and their auto-correlation characteristics during the whole time period. However, similar results are obtained for R_{cri}=0.999 (*RMF*: 46.1% for DRBTO and UDRTO). Since the displacement at only one moment will surpass the displacement

threshold, the responses tracked by the two schemes are identical, but the reliability index is defined differently. The reliability verification of topology configuration shows that all the results meet the NTR constraints. To sum up, the proposed DRBTO scheme can truly reflect the time-dependency properties and further ensure the validity of the optimal topology.

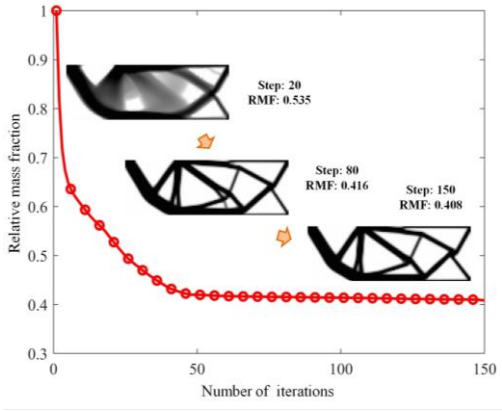

(a) DRTO

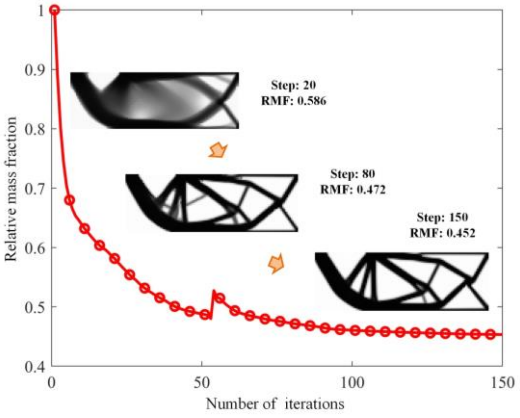

(b) DRBTO (R_{cri} =0.95)

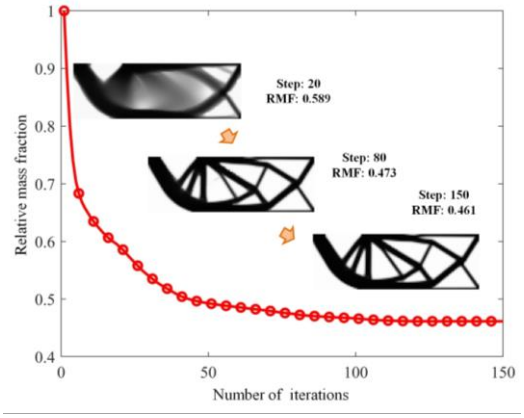

(c) DRBTO (R_{cri} =0.999)

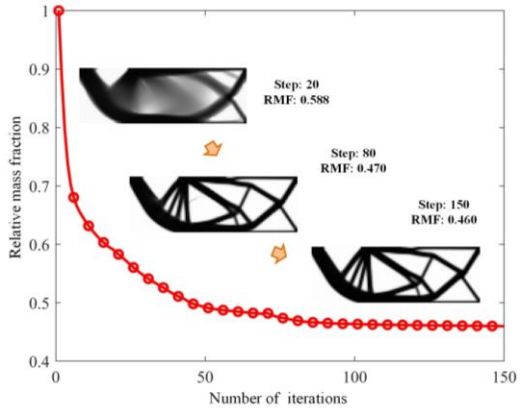

(d) UDRTO (R_{cri} =0.95)

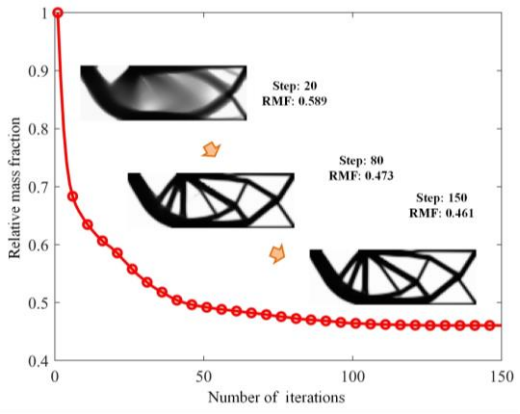

(e) UDRTO (R_{cri} =0.999)

Fig. 9 Iteration histories with different optimization strategies

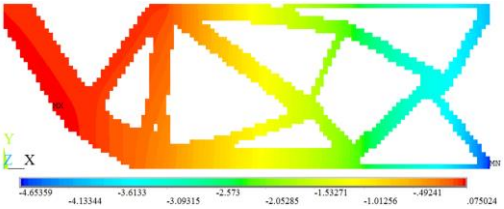

(a) DRTO

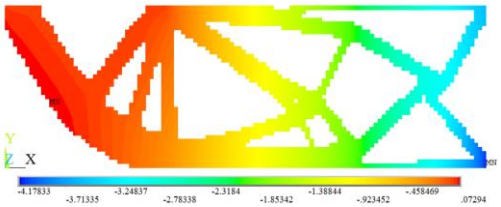

(b) DRBTO (R_{cri} =0.95)

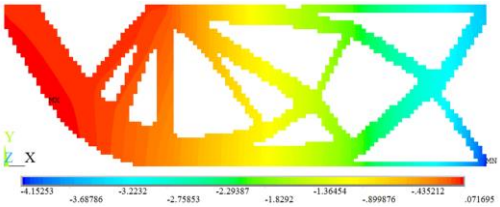

(c) DRBTO (R_{cri} =0.999)

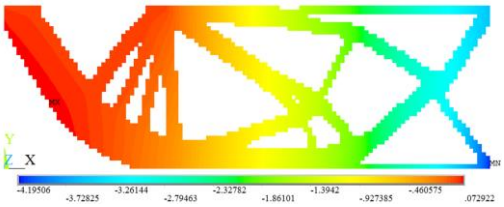

(d) UDRTO (R_{cri} =0.95)

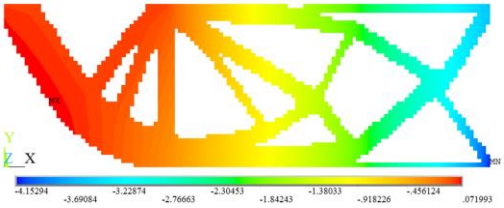

(e) UDRTO (R_{cri} =0.999)

Fig. 10 Optimization layouts with different optimization strategies

Table 3 The values of *RMF* and verified NTR of all final topology structures

Values	**DRTO**	**DRBTO** (R_{cri} =0.95)	**DRBTO** (R_{cri} =0.999)	**UDRTO** (R_{cri} =0.95)	**UDRTO** (R_{cri} =0.999)
RMF	0.408	0.452	0.461	0.460	0.461
NTR of u_x	-	0.9559	1.0004	0.9612	1.0007
NTR of u_y	-	0.9598	0.9998	0.9678	1.0002

Table 4 Dynamic responses of optimization structures with different optimization strategies

Responses	**Displacement responses**	**Velocity responses**	**Acceleration responses**
DRTO	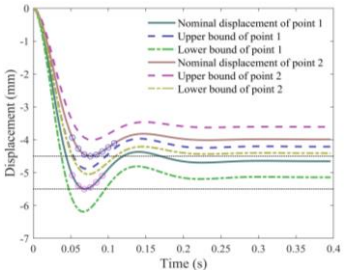	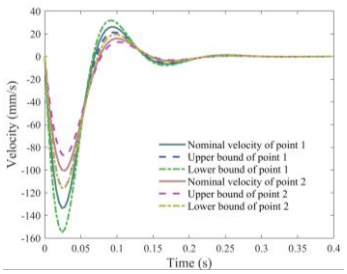	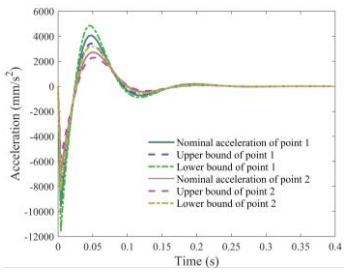
DRBTO (R_{cri} =0.95)	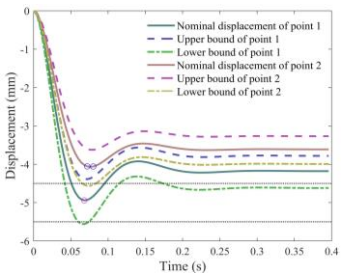	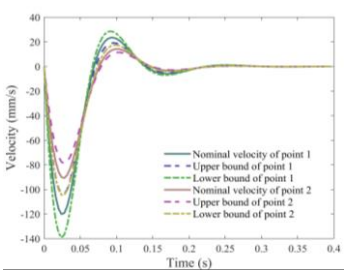	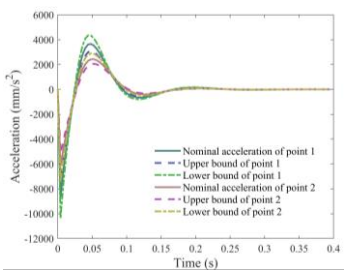

DRBTO (R_{cri}=0.999)

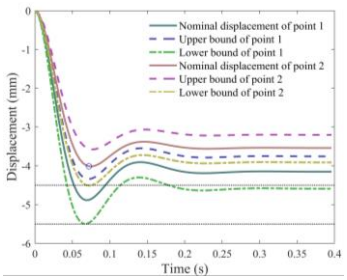

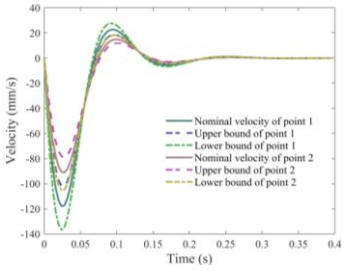

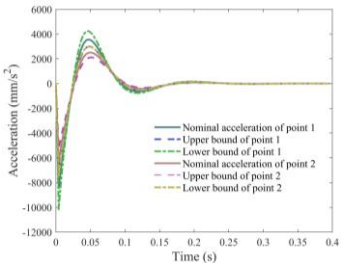

UDRTO (R_{cri}=0.95)

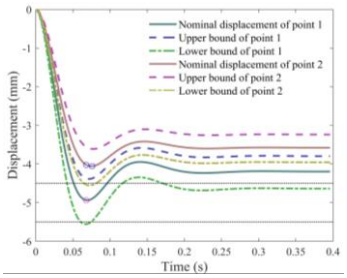

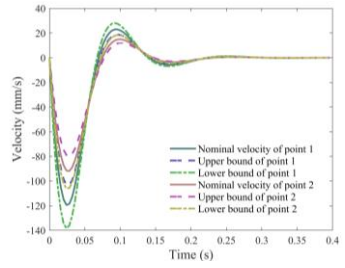

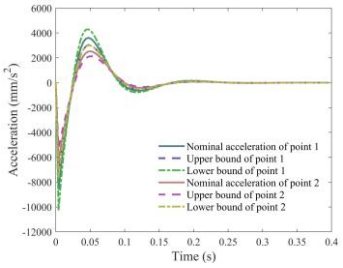

UDRTO (R_{cri}=0.999)

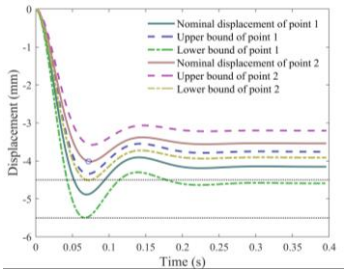

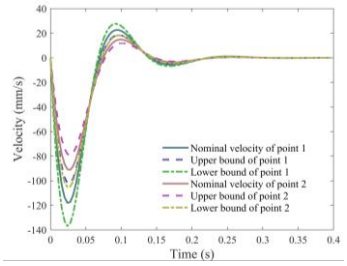

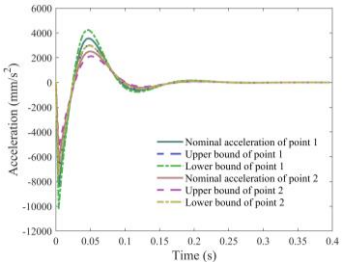

4. As can be seen from Table 5, the final optimal configurations are identical when ε_2 is set as $1/10$, $1/20$ and $1/40$ for the DRTO and DRBTO schemes. It clearly implies that the optimization processes have entered into a state of convergence both in configuration itself or the intermediate densities elements, when the proportion of concerned elements (whose density variation not less than 10^{-3}) is not more than $1/10$. While for the UDRTO, the convergent configuration may be obtained when ε_2 is set as $1/20$. Although there is an oscillation for DRBTO (R_{cri}=0.95) as shown in Fig. 9, the DRBTO converges more easily than the UDRTO.

Table 5 The final optimal configuration with different convergence tolerance

ε_2	**1/3**	**1/5**	**1/10**	**1/20**	**1/40**
DRTO	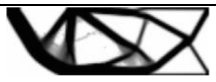				
DRBTO R_{cri}=0.95	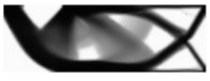				
DRBTO R_{cri}=0.999					
UDRTO R_{cri}=0.95					
UDRTO R_{cri}=0.999					

6.2 Optimization for a L-shaped plate structure

A L-shaped plate structure which is meshed with equally discretized 2000 four-node elements is studied in this example. Its geometric dimension is displayed in Fig. 11 (a) and the thickness is set as 1mm. Its underside is supported and 2 dynamic forces are imposed to the bottom of the right side in the x and y direction (as demonstrated in Fig. 11 (b)), and timestep is consistent with that used in example 1. Different levels of uncertainties, namely, small uncertainty, medium uncertainty, and large uncertainty, are introduced in each type of optimization process, for whose deterministic values and marginal intervals are listed in Table 6. Furthermore, the structural density of solid material is set as $7800\ \mathrm{kg/m^3}$, the Poisson's ratio is set as 0.3, and the damping coefficient of mass set as 0. In the DRTO and DRBTO model, the allowable displacements u_{cri}^{x} and u_{cri}^{y} in the x and y direction are both taken as $-1.8\ \mathrm{mm}$, and the reliability thresholds are both set $R_{cri}^{x}=R_{cri}^{y}=0.999$. The convergence numbers are specified as $\varepsilon_1=10^{-3}$ and $\varepsilon_2=1/20$ based in the convergence results in Section 6.1.

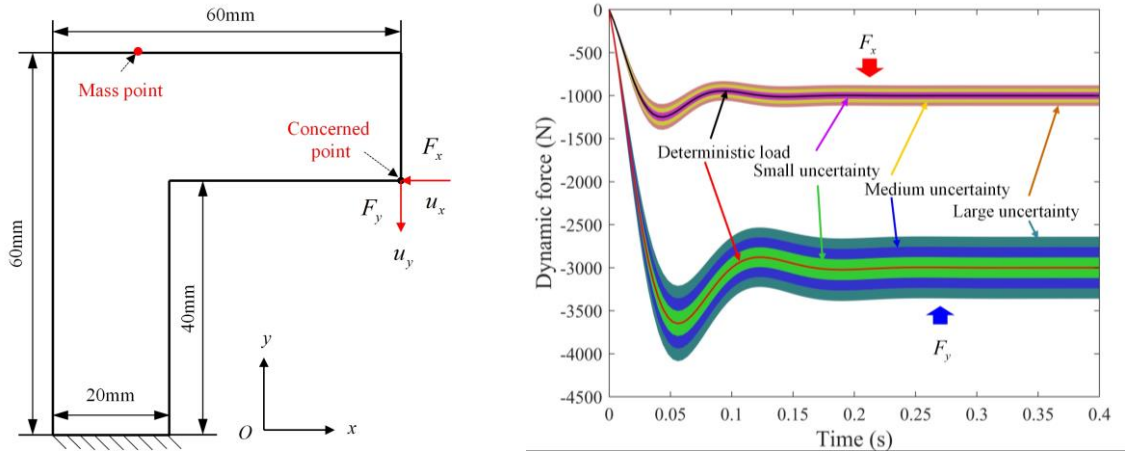

(a) The L-shaped plate structure (b) The time-variant load

Fig. 11 Design domain and boundary conditions

Table 6 Uncertain characteristics of the L-shaped plate structure

Parameters	Deterministic value	Small uncertainty	Medium uncertainty	Large uncertainty
E^I (GPa)	210	$[201.6, 218.4]$	$[193.2, 226.8]$	$[184.8, 235.2]$
β^I	0.02	[0.0192, 0.0208]	[0.0184, 0.0216]	[0.0176, 0.0224]
M_{mass}^I (kg)	0.5	[0.48, 0.52]	[0.46, 0.54]	[0.44, 0.56]
F_x^I (N)	F_x^c	$\left[0.96F_x^c, 1.04F_x^c\right]$	$\left[0.92F_x^c, 1.08F_x^c\right]$	$\left[0.88F_x^c, 1.12F_x^c\right]$
F_y^I (N)	F_y^c	$\left[0.96F_y^c, 1.04F_y^c\right]$	$\left[0.92F_y^c, 1.08F_y^c\right]$	$\left[0.88F_y^c, 1.12F_y^c\right]$
Fluctuating level		8%	16%	24%

The iteration histories with different uncertain parameters are shown in Fig. 12. For the obtained topology structure, the cloud atlas of resultant nominal displacements at 0.4s and the force-carrying state of generated members are illustrated in Fig. 13, the history of dynamic responses of the concerned point in the x and y direction under 4 parameter settings are listed in Table 7, the values of *RMF* and verified NTR of all final topology structures are observed in Table 8, and the comparisons of maximum displacement responses of concerned point are summarized in Table 9. Based on our results and findings, it can be concluded that:

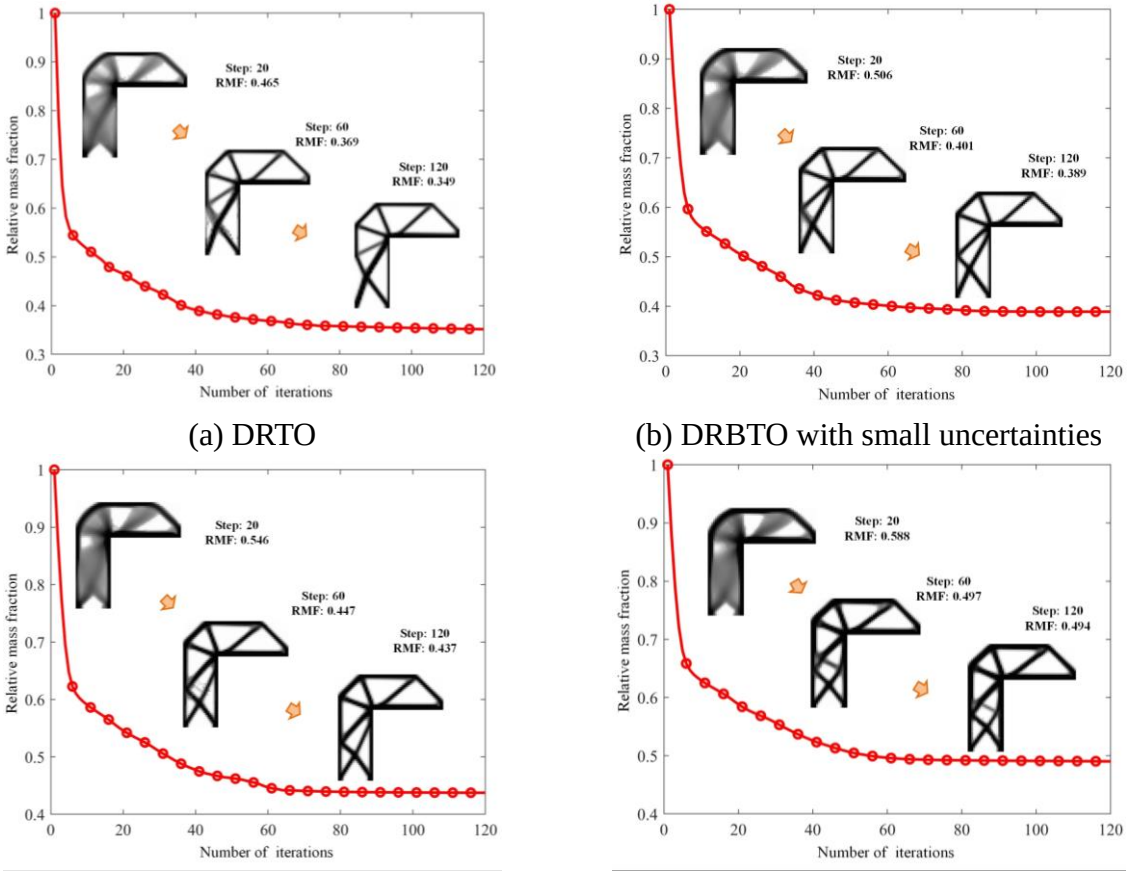

(a) DRTO (b) DRBTO with small uncertainties

(c) DRBTO with medium uncertainties (d) DRBTO with large uncertainties

Fig. 12 Iteration histories with different uncertainties

1. Identical conclusions are drawn with that given in example 1. The loading path of the topological structure obtained by DRTO does not agree with that given by DRBTO. The positions with obvious differences in four configurations have been marked in red circles in Fig. 13. We can see that higher levels of uncertainties yield larger undulations of mechanical behaviors and consequently more robust layout and greater *RMF*. For example, a vertical bar will be created below the left side of the L-shaped plate structure for the 3 DRBTO strategies to prevent too much displacement of u_x caused by uncertainties. Moreover, the layout of load-carrying bars in the half bottom is also different, and an additional bar is produced for

the DRBTO with large uncertainties. Thus, the structural force-carrying states are slightly different from each other. As shown in Fig. 13, the generated elements in subfigure (d) are the strongest and the loading paths are also the most complex.

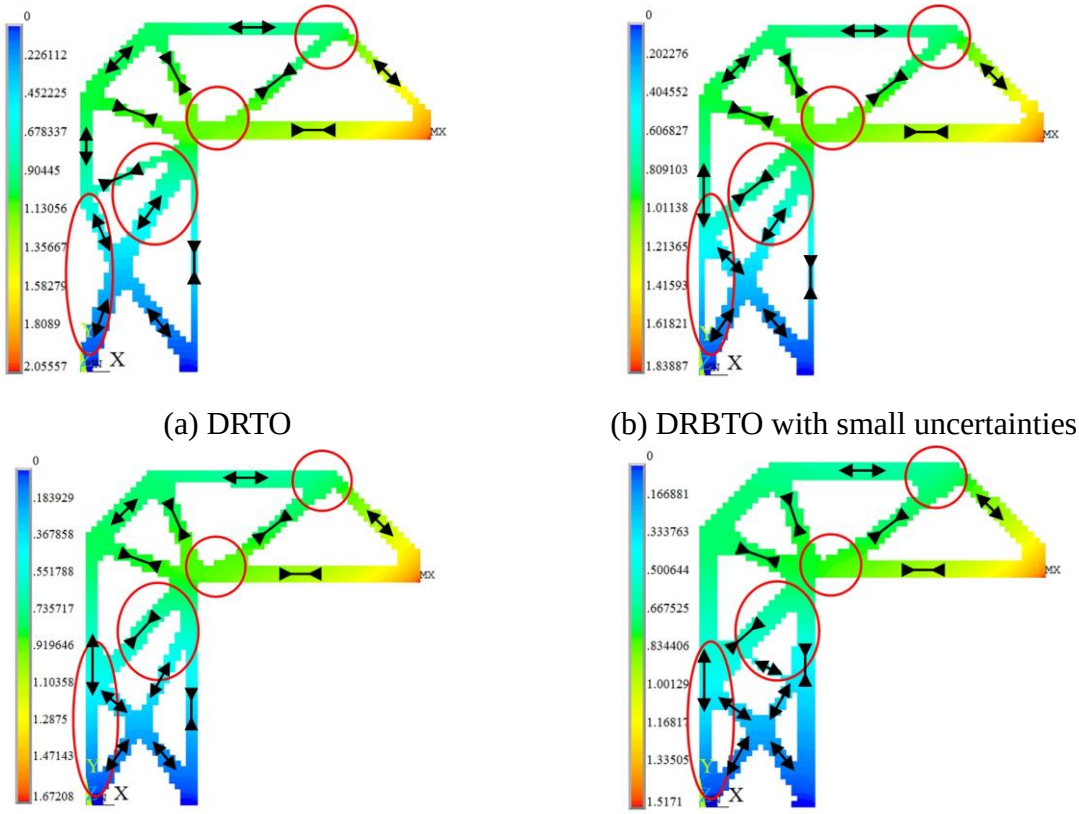

(a) DRTO (b) DRBTO with small uncertainties

(c) DRBTO with medium uncertainties (d) DRBTO with large uncertainties

Fig. 13 Optimization layouts with different uncertainties

2. As indicated in Table 8, the *RMF* increment calculated by the *RMF* of 3 DRBTO strategies minus the *RMF* of DRTO scheme is disproportionate under proportionable uncertainty levels of 4%, 8% and 12% for final topological structures, which is $0.389-0.349=0.04$, $0.437-0.349=0.088$, and $0.494-0.349=0.145$. Furthermore, the NTR indices of the concerned displacements of all optimized configurations are greater than the desired $R_{cri}^{x}=R_{cri}^{y}=0.999$.

3. As shown in Table 7 and Table 9, the sensitivities of two-directional dynamic responses with respect to uncertainties are difficult. For example, the displacement fluctuations along the y direction are larger than those along the x direction. Moreover, the nominal dynamic responses of structures obtained by DRBTO are less than those obtained by DRTO. This phenomenon becomes more obvious with the increase of uncertainty levels (u_x: -1.5872 mm for small uncertainties, -1.4334 mm for medium uncertainties,

-1.2966 mm for large uncertainties; u_y : -1.4719 mm for small uncertainties, -1.2750 mm for medium uncertainties, -1.1275 mm for large uncertainties). The fluctuation levels of the maximum displacements are also non-linear with the uncertainty levels.

Table 7 Dynamic responses of optimization structure with different uncertainties

Responses	**Displacement responses**	**Velocity responses**	**Acceleration responses**
DRTO	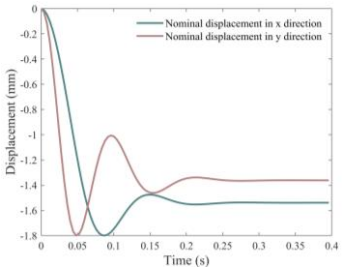	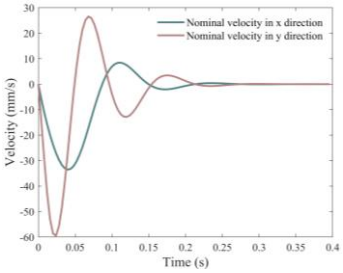	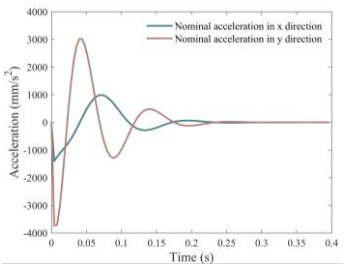
DRBTO with small uncertainties	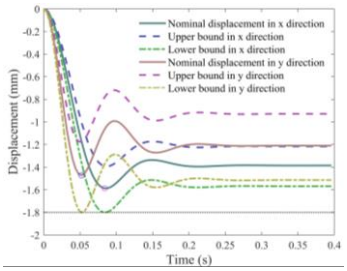	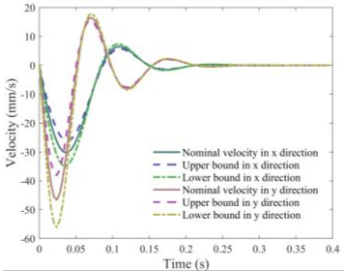	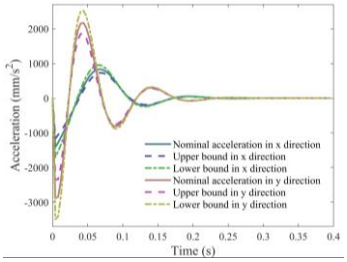
DRBTO with medium uncertainties	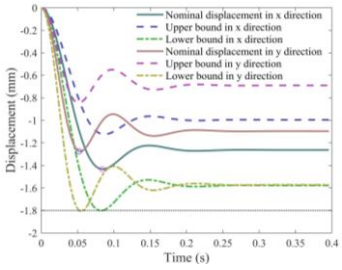	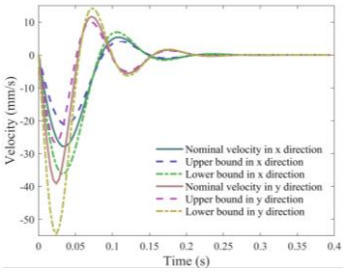	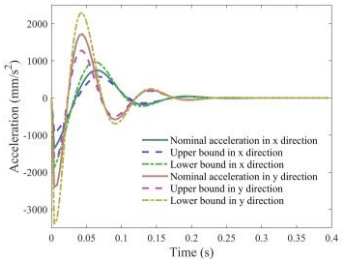
DRBTO with large uncertainties	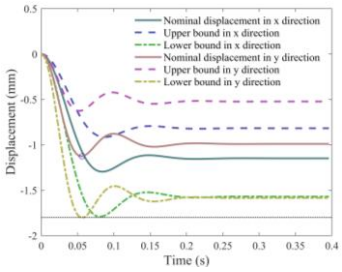	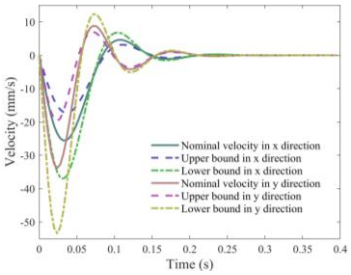	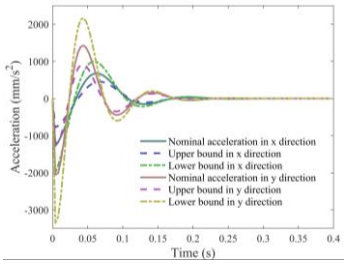

Table 8 The values of *RMF* and verified NTR of all final topology structures

Values	**DRTO**	**DRBTO with small uncertainties**	**DRBTO with medium uncertainties**	**DRBTO with large uncertainties**
RMF	0.349	0.389	0.437	0.494
NTR of u_x	-	0.9993	0.9991	1.0057
NTR of u_y	-	0.9996	0.9991	1.0179

Table 9 Maximum displacement responses of concerned point with different uncertainties

Maximum displacement		DRTO	DRBTO with small uncertainties	DRBTO with Medium uncertainties	DRBTO with large uncertainties
u_x	Nominal displacement (mm)	-1.7997	-1.5872	-1.4334	-1.2966
	Upper bound (mm)	--	-1.3929	-1.1241	-0.9149
	Lower bound (mm)	--	-1.8002	-1.8006	-1.7924
	Fluctuation level (%)	--	25.66	47.20	67.68
u_y	Nominal displacement (mm)	-1.7999	-1.4719	-1.275	-1.1275
	Upper bound (mm)	--	-1.1752	-0.8454	-0.6274
	Lower bound (mm)	--	-1.8004	-1.8078	-1.805
	Fluctuation level (%)	--	42.48	75.48	104.44

6.3 Optimization for a wing rib structure

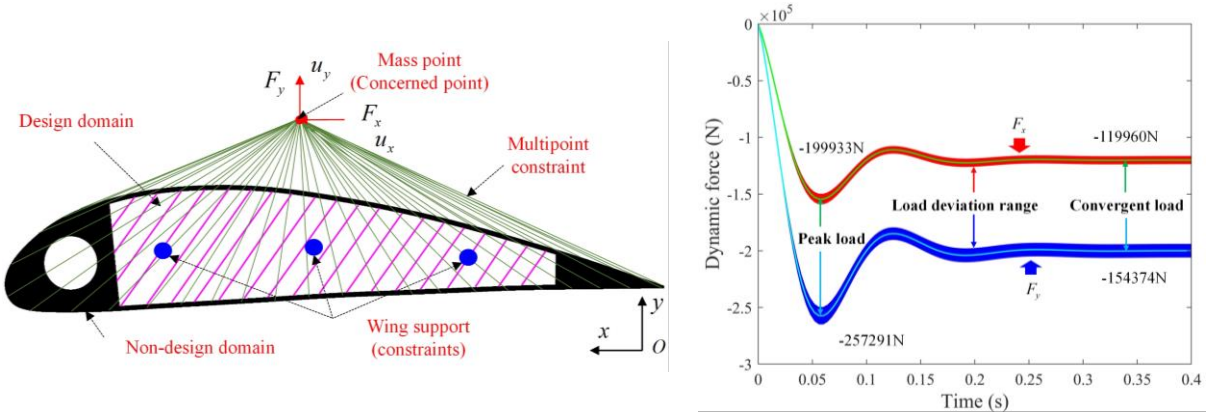

(a) The wing rib structure (b) The time-variant load

Fig. 14 Design domain and boundary conditions

Table 10 Uncertain characteristics of the rectangular plate structure

Parameters	E^I (GPa)	β^I	F_x^I (N)	F_y^I (N)
Values	$[142.5, 157.5]$	$[0.018, 0.022]$	$[0.97F_1^c, 1.03F_1^c]$	$[0.97F_2^c, 1.03F_2^c]$
Fluctuating level	10%	20%	6%	6%

To better demonstrate the capability of the presented DRNTO framework when dealing with complex engineering problems, a wing rib structure as shown in Fig. 14 (a), is studied. Three small structural constraints near the center of the wing model are involved to simulate wing-box attachment. The internal space of the wing rib marked with magenta lines is manipulated as the TO design domain, while the leading edge, trailing edge, edge strip of the wing rib filled with black and blue supports are considered as the non-design domain. Particularly, the skin is arranged as a non-design space in order to maintain the aerodynamic

shape of the airfoil. For simplicity, aerodynamic forces are replaced by 2 concentrated loads through a flexible-connected multipoint constraint around the wing structure. The horizontal load F_x and vertical load F_y applied to the mass point can be transferred to all FEM nodes on the outer of skins, whose variation trends are plotted in Fig. 14 (b).

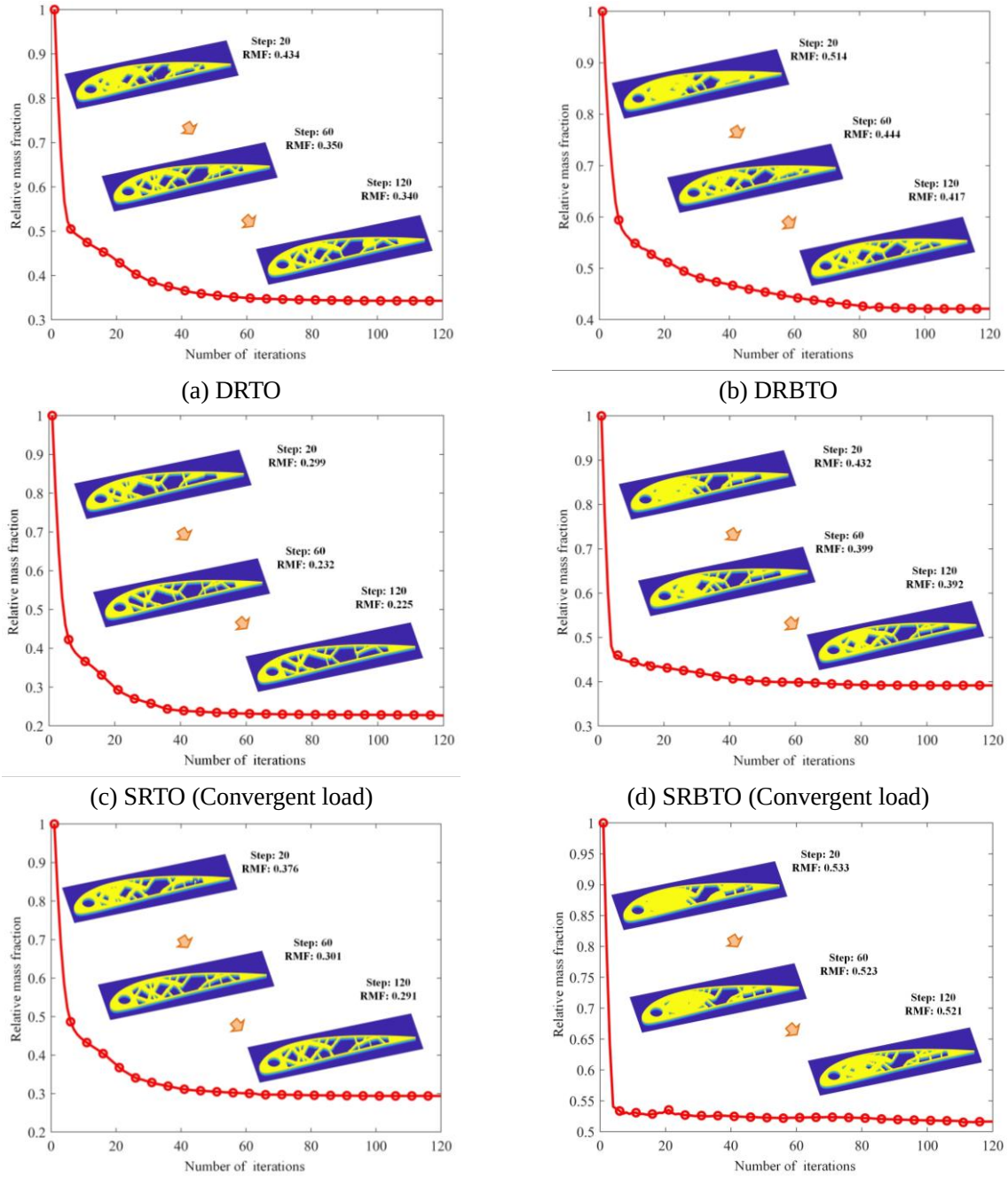

(a) DRTO (b) DRBTO

(c) SRTO (Convergent load) (d) SRBTO (Convergent load)

(e) SRTO (Peak load) (f) SRBTO (Peak load)

Fig. 15 Iteration histories with different optimization strategies

To illustrate the necessity and superiority of DRTO and DRBTO to perform the dynamic design of material layout, the static design scheme proposed by Ref. [57] is implemented as

well, including the static response TO (SRTO) and the static reliability-based TO (SRBTO). The Young's modulus, structural density and the Poisson's ratio for the solid phases are 150 GPa , 2700 kg/m^3 and 0.3, respectively. Considering the damping factor in dynamics, it is assumed that α=0 and β=0.02 . It can be seen that the load F_x converges to -119960 N and F_y converges to -154374 N . The peak value of F_x is -199933 N and peak value of F_y is -257291 N . Hence, two static conditions (the convergent loads and peak loads) are employed. In addition, the details of uncertainties are listed in Table 10. However, the uncertainty of β is ignored in the case of SRBTO. For the strategies of DRTO, DRBTO, SRTO and SRBTO, the displacements u_x and u_y of the mass point is defined as the concerned responses with criteria $u_{cri}^x = -5$ mm and $u_{cri}^y = -15$ mm . For the optimization strategies of DRBTO and SRBTO, the threshold of reliability level is set to $R_{cri} = 0.999$. The condition of convergence is set as ε_1=10^{-3} and ε_2=$1/20$.

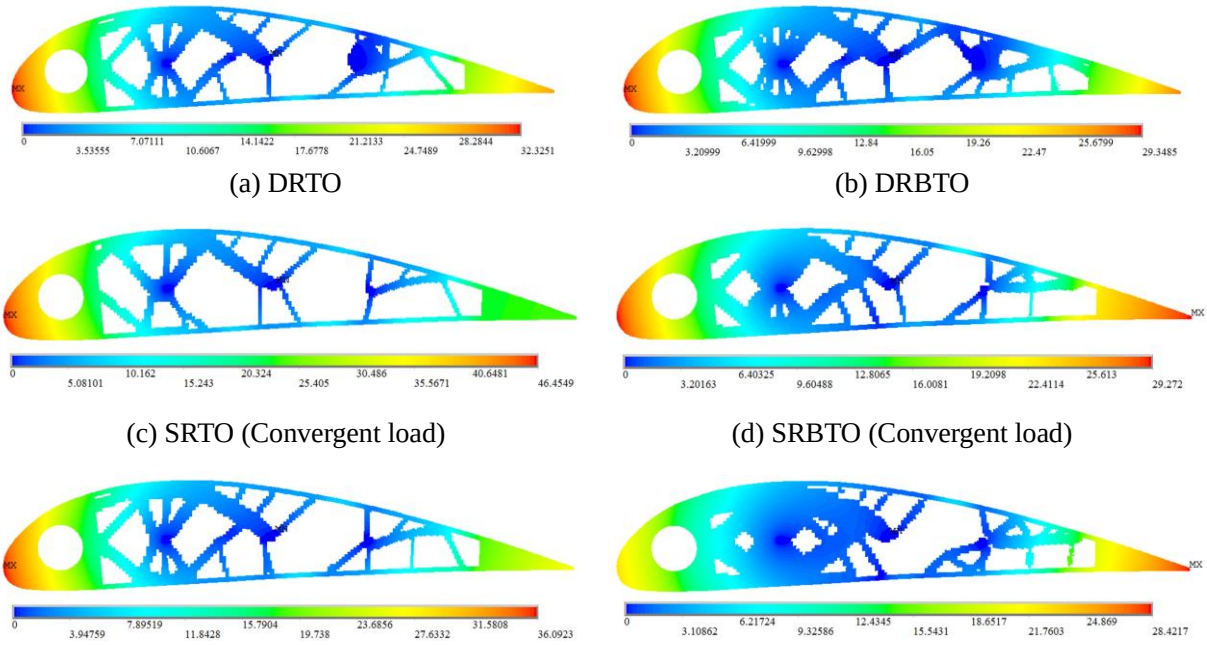

(a) DRTO (b) DRBTO

(c) SRTO (Convergent load) (d) SRBTO (Convergent load)

(e) SRTO (Peak load) (f) SRBTO (Peak load)

Fig. 16 Optimization layouts with different optimization strategies

Table 11 Dynamic responses of optimization structures with different optimization strategies

Responses	Displacement responses	Velocity responses	Acceleration responses
DRTO	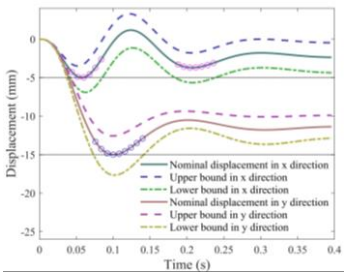	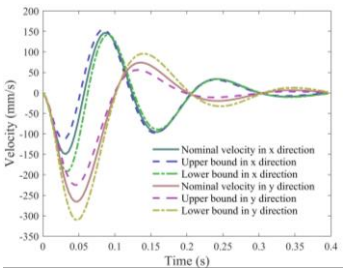	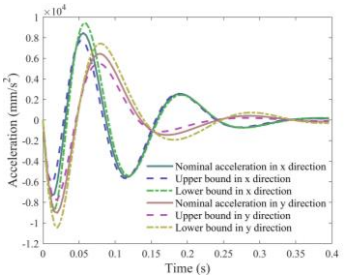

DRBTO

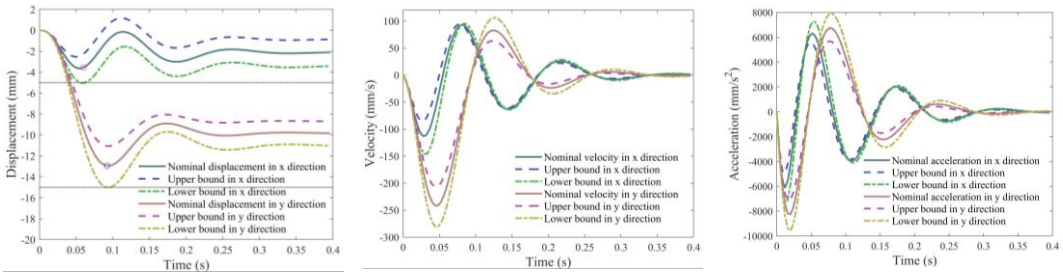

SRTO (Converg-ent load)

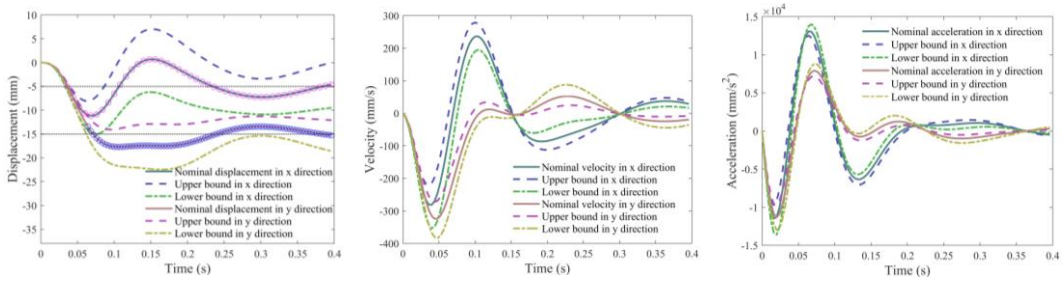

SRBTO (Converg-ent load)

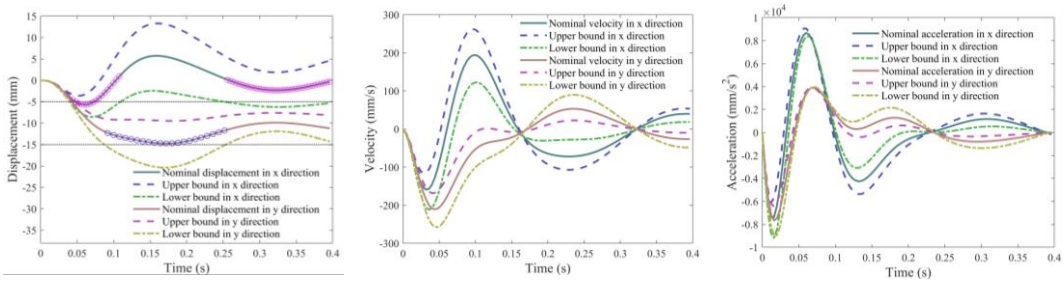

SRTO (Peak load)

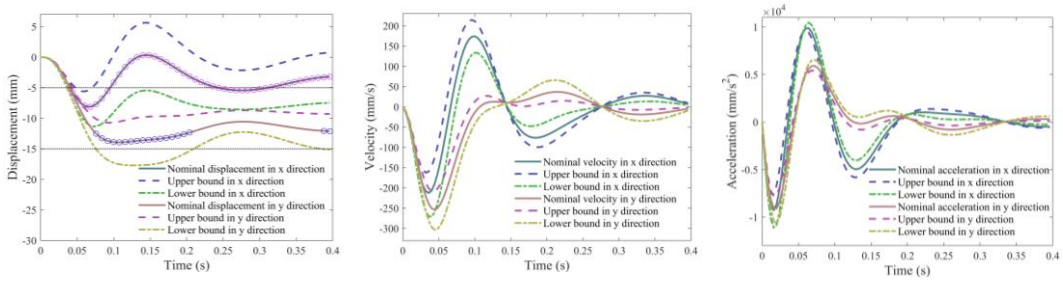

SRBTO (Peak load)

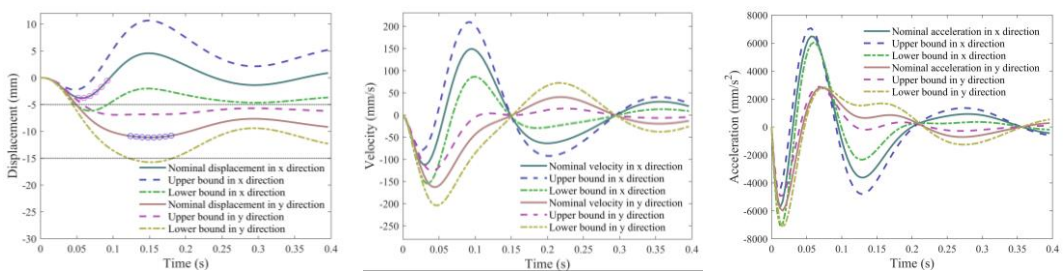

The optimization results are presented in Fig. 15, and the cloud atlas of resultant nominal displacements at 0.4s are manifested in Fig. 16. Carrying out dynamic FEM simulations under uncertainty conditions, the displacement, velocity, and acceleration responses of the mass point of optimization structures with different optimization strategies are listed in Table 11. Under the static case of peak load, the displacements of the mass point of different topology structures are summarized in Table 12. From the results given above, the following points can be concluded:

1. From Fig. 15 and Fig. 16, there are remarkable discrepancies between the load-transferring paths obtained by diverse optimization strategies with different constraint criteria. For the deterministic optimization, the final configuration from DRTO (*RMF*=0.340) is heavier than that from SRTO (*RMF*=0.225 for convergent loads and *RMF*=0.291 for peak loads). When the uncertainties are considered, the optimization rules are quite different due to different definitions of reliability judgements. The *RMF* of topology structures from DRBTO (*RMF*=0.417) is not higher than that from SRBTO (*RMF*=0.392 for convergent loads and *RMF*=0.521 for peak loads). It is worth noting that a block of solid is generated near the right constraint for dynamic TOs.

2. As revealed in Table 11, the responses of dynamic designs are smaller than those of static designs either deterministic optimization or reliability-based optimization. Moreover, the structural responses obtained by dynamic optimization possess much better convergence rate and stability. For example, the displacement responses approximately converge in 0.3s for DRTO and 0.25s for DRBTO, while they are not stable in the whole loading history. It follows that the dynamic designs outperform their static counterpart in terms of dynamic performances. It may be explained that many factors like the inertia/damping characteristics, some excessive displacements in the entire process caused by time-varying loads are not taken into account in the SRTO strategy.

Table 12 The static displacement under peak load with different topology structures

Displacement responses	u_x **(mm)**			u_y **(mm)**		
	Nominal displacement	**Upper bound**	**Lower bound**	**Nominal displacement**	**Upper bound**	**Lower bound**
DRTO	-2.8753	-0.4842	-5.4010	-14.7593	-12.7845	-16.8306
DRBTO	-2.7188	-1.1269	-4.4075	-12.6318	-11.1741	-14.1687
SRTO (Convergent load)	-6.4346	-0.5944	-12.4965	-19.2999	-15.4039	-23.3114
SRBTO (Convergent load)	0.8984	8.0161	-6.4509	-14.6836	-10.1530	-19.3125
SRTO (Peak load)	-5.0005	-0.0936	-10.0831	-14.9998	-11.7566	-18.3321
SRBTO (Peak load)	0.5395	5.9520	-5.0094	-11.3983	-7.8533	-15.0100

3. Performing uncertain FEM analysis under the risky static cases of peak loads, only the lower bounds of the structures from DRBTO ($\underline{u}_x = -4.4075$ mm and $\underline{u}_y = -14.1687$ mm) and SRBTO with peak load ($\underline{u}_x = -5.0094$ mm and $\underline{u}_y = -15.0100$ mm) strategies can meet the requirement of the reliability constraints. The lower bounds of concerned displacements

by the DRTO scheme ($\underline{u}_x = -5.4010$ mm and $\underline{u}_y = -16.8306$ mm) slightly exceed the displacement threshold value, but the displacements by other three static optimizations far exceed the displacement criteria as revealed by Table 12. One unanticipated finding is that the topology configuration based on the DRBTO strategy can be applied to more situations.

7 Conclusions

In view of the practical engineering demands, considering multi-source uncertainties into dynamic response TO problems plays an important role structural design. It leads to the systematic research on DRBTO framework, which has become a research hotspot for future development of intelligent design technologies. Current layout design methodologies, however, mainly have two typical shortages: (1) the quasi-static simplification treatments in topological configuration with no time-dependent factors; (2) the statistical-quantitative uncertainty models and reliability definitions without consideration of sampling limitation for failure probability solutions. Consequently, the non-probabilistic and time-variant design optimization scheme should be further explored.

As revealed by the above issues, a new DRBTO framework, which combines the non-probabilistic interval mathematics and time-variant out-crossing reliability ideas, is developed in this study. Major novel contributions of this paper lie in: (1) the interval-process collocation theorem is proposed to effectively achieve uncertain transient analysis during each topological iteration; (2) the first-passage model for local stiffness failure is established and the non-probabilistic time-variant reliability (NTR) index is analyzed; (3) the NTR-based sensitivity updating mechanism for large-scale design variables is expounded in details by virtue of the adjoint equation and the density filtering policy. Numerical examples demonstrate the effectiveness of the presented research, and they also show that the uncertain and dynamic effects both have great influences on the design results.

Nevertheless, compared with the traditional RBTO methods that are applying for static problems, performing the DRBTO design process is more complicated. The developed methodologies in this paper could be an effective supplement to existing research works. Based on this work, studying further issues, such as the multi-functional and multi-scale design conditions, will be the following research topics in our future work.

Acknowledgements

The authors would like to thank National Nature Science Foundation of China (12072007) and the EU Marie Sklodowska-Curie Individual Fellowships

(H2020-MSCA-IF-2020:101025743-ROFiDMS) for the financial supports. Besides, the authors wish to express their many thanks to the reviewers for their useful and constructive comments.

Appendix A

Referring to Eq. (7), Eq. (9) can be transformed into two normalization expressions

$$u_i(\mathbf{x},\ t_1) \in \left[\underline{u}_i(\mathbf{x},\ t_1),\ \overline{u}_i(\mathbf{x},\ t_1)\right] = u_{i0}(\mathbf{x},\ t_1) + u_{ir}(\mathbf{x},\ t_1) \circ \zeta_{u_i}(t_1) \tag{51}$$

and

$$u_i(\mathbf{x},\ t_2) \in \left[\underline{u}_i(\mathbf{x},\ t_2),\ \overline{u}_i(\mathbf{x},\ t_2)\right] = u_{i0}(\mathbf{x},\ t_2) + u_{ir}(\mathbf{x},\ t_2) \circ \zeta_{u_i}(t_2) \tag{52}$$

where

$$u_{i0}(\mathbf{x},\ t_\kappa) = \frac{\overline{u}_i(\mathbf{x},\ t_\kappa) + \underline{u}_i(\mathbf{x},\ t_\kappa)}{2} \quad \text{and} \quad u_{ir}(\mathbf{x},\ t_\kappa) = \frac{\overline{u}_i(\mathbf{x},\ t_\kappa) - \underline{u}_i(\mathbf{x},\ t_\kappa)}{2} \tag{53}$$

And $\zeta_{u_i}(t_1)$, $\zeta_{u_i}(t_2)$ are standard intervals corresponding to $u_i(\mathbf{x},\ t_1)$ and $u_i(\mathbf{x},\ t_2)$. As shown in Fig. 3, countless deflected rectangles may be generated intersecting the boundaries of the standard square when the two diagonal lines are taken as the centerline. They have diverse shapes with different characteristic length $d_{u_i}(t_1,\ t_2)$ in $\zeta_{u_i}(t_1)$ - $\zeta_{u_i}(t_2)$ space. Moreover, the $d_{u_i}(t_1,\ t_2)$ can vividly reflect the correlation between interval variables $u_i(\mathbf{x},\ t_1)$ and $u_i(\mathbf{x},\ t_2)$. Taking several typical situations as examples, the correlation coefficient is equal to 0 and the rotated rectangle has the maximum area for situation ③, while the correlation coefficient is 1/-1 and the rectangles degenerate into the diagonal lines for situation ① and ⑤. It means that the absolute value of the correlation coefficient increases with the rectangular becomes longer and narrower.

References

[1] M. Cavazzuti, A. Baldini, E. Bertocchi, D. Costi, E. Torricelli, High performance automotive chassis design: a topology optimization based approach, Structural and Multidisciplinary Optimization, 44 (2011) 45-56.

[2] J.H. Zhu, W.H. Zhang, L. Xia, Topology optimization in aircraft and aerospace structures design, Archives of Computational Methods in Engineering, 23 (2016) 595-622.

[3] H.N. Lopes, J. Mahfoud, R. Pavanello, High natural frequency gap topology optimization of bi-material elastic structures and band gap analysis, Structural and Multidisciplinary Optimization, 63 (2021) 2325-2340.

[4] Y. Maeda, S. Nishiwaki, K. Izui, M. Yoshimura, K. Terada, Structural topology optimization of vibrating structures with specified eigenfrequencies and eigenmode shapes, International Journal for Numerical Methods in Engineering, 67 (2006) 597-628.

[5] R. Picelli, W.M. Vicente, R. Pavanello, Y.M. Xie, Evolutionary topology optimization for natural frequency maximization problems considering acoustic–structure interaction, Finite Elements in Analysis and Design, 106 (2015) 56-64.

[6] J.P. Zhao, C.J. Wang, Dynamic response topology optimization in the time domain using model reduction method, Structural and Multidisciplinary Optimization, 53 (2016) 101-114.

[7] F. Valentini, O.M. Silva, E.L. Cardoso, Robust topology optimization for harmonic displacement minimization of structures subjected to uncertainty in the excitation frequency, Computer Methods in Applied Mechanics and Engineering, 379 (2021) 113767.

[8] S. Min, N. Kikuchi, Y.C. Park, S. Kim, S. Chang, Optimal topology design of structures under dynamic loads, Structural optimization, 17 (1999) 208-218.

[9] H.H. Jang, H.A. Lee, J.Y. Lee, G.J. Park, Dynamic response topology optimization in the time domain using equivalent static loads, AIAA journal, 50 (2012) 226-234.

[10] X.P. Zhang, Z. Kang, Dynamic topology optimization of piezoelectric structures with active control for reducing transient response, Computer Methods in Applied Mechanics and Engineering, 281 (2014) 200-219.

[11] F. Gomez, B.F. Spencer, Topology optimization framework for structures subjected to stationary stochastic dynamic loads, Structural and Multidisciplinary Optimization, 59 (2019) 813-833.

[12] L. Zhao, B. Xu, Y.S. Han, Y.M. Xie, Topology optimization of dynamic stress response reliability of continuum structures involving multi-phase materials, Structural and Multidisciplinary Optimization, 59 (2019) 851-876.

[13] J.P. Zhao, C.J. Wang, Topology optimization for minimizing the maximum dynamic response in the time domain using aggregation functional method, Computers and Structures, 190 (2017) 41-60.

[14] L. Wang, Y.R. Liu, Y.S. Liu, An inverse method for distributed dynamic load identification of structures with interval uncertainties, Advances in Engineering Software, 131 (2019) 77-89.

[15] L. Wang, Y.R. Liu, A novel method of distributed dynamic load identification for aircraft structure considering multi-source uncertainties, Structural and Multidisciplinary Optimization, 61 (2020) 1929-1952.

[16] C. Yang, X.B. Hou, S.N. Chang, A synchronous placement and size-based multi-objective optimization method for heat dissipation design on antenna module of space solar power satellite, Sustainable Energy Technologies and Assessments, 45 (2021) 101183.

[17] D.L. Liu, Z.P. Qiu, A subinterval dimension-wise method for robust topology optimization of structures with truss-like lattice material under unknown but bounded uncertainties, Structural and Multidisciplinary Optimization, (2021) 1-18.

[18] G.A. da Silva, E.L. Cardoso, A.T. Beck, Comparison of robust, reliability-based and non-probabilistic topology optimization under uncertain loads and stress constraints, Probabilistic Engineering Mechanics, 59 (2020) 103039.

[19] Z.C. He, Y. Wu, E. Li, Topology optimization of structure for dynamic properties considering hybrid uncertain parameters, Structural and Multidisciplinary Optimization, 57 (2018) 625-638.

[20] L. Alacoque, R.T. Watkins, A.Y. Tamijani, Stress-based and robust topology optimization for thermoelastic multi-material periodic microstructures, Computer Methods in Applied Mechanics and Engineering, 379 (2021) 113749.

[21] B. Ahmadi, M. Jalalpour, A. Asadpoure, M. Tootkaboni, Robust topology optimization of skeletal structures with imperfect structural members, Structural and Multidisciplinary Optimization, 58 (2018) 2533-2544.

[22] S. Bobby, A. Suksuwan, S.M.J. Spence, A. Kareem, Reliability-based topology optimization of uncertain building systems subject to stochastic excitation, Structural Safety, 66 (2017) 1-16.

[23] Z. Meng, G. Li, X. Wang, S.M. Sait, A.R. Yıldız, A comparative study of metaheuristic algorithms for reliability-based design optimization problems, Archives of Computational Methods in Engineering, 28 (2021) 1853-1869.

[24] L. Wang, Y.R. Liu, K.X. Gu, T. Wu, A radial basis function artificial neural network (RBF ANN) based method for uncertain distributed force reconstruction considering signal noises and material dispersion, Computer Methods in Applied Mechanics and Engineering, 364 (2020) 112954.

[25] Y.R. Liu, L. Wang, Z.P. Qiu, X. Chen, A dynamic force reconstruction method based on modified Kalman filter using acceleration responses under multi-source uncertain samples, Mechanical Systems and Signal Processing, 159 (2021) 107761.

[26] C. Yang, A novel uncertainty-oriented regularization method for load identification, Mechanical Systems and Signal Processing, 158 (2021) 107774.

[27] Z. Meng, Y.S. Pang, Y.X. Pu, X. Wang, New hybrid reliability-based topology optimization method combining fuzzy and probabilistic models for handling epistemic and aleatory uncertainties, Computer Methods in Applied Mechanics and Engineering, 363 (2020) 112886.

[28] Z. Meng, Y. Wu, X. Wang, S.H. Ren, B. Yu, Robust topology optimization methodology for continuum structures under probabilistic and fuzzy uncertainties, International Journal for Numerical Methods in Engineering, 122 (2021) 2095-2111.

[29] S. Sleesongsom, S. Bureerat, Multi-objective reliability-based topology optimization of structures using a fuzzy set model, Journal of Mechanical Science and Technology, 34 (2020) 3973-3980.

[30] Y. Ben-Haim, A non-probabilistic concept of reliability, Structural safety, 14 (1994) 227-245.

[31] Y.J. Luo, K. Zhan, L. Zhen, A. Li, Continuum topology optimization with non-probabilistic reliability constraints based on multi-ellipsoid convex model, Structural and Multidisciplinary Optimization, 39 (2009) 297-310.

[32] Z. Kang, Y.J. Luo, Non-probabilistic reliability-based topology optimization of geometrically nonlinear structures using convex models, Computer Methods in Applied Mechanics and Engineering, 198 (2009) 3228-3238.

[33] R.B. dos Santos, A.J. Torii, A.A. Novotny, Reliability‐based topology optimization of structures under stress constraints, International Journal for Numerical Methods in Engineering, 114 (2018) 660-674.

[34] M. Li, W.C. Tang, M. Yuan, Structural dynamic topology optimization based on dynamic reliability using equivalent static loads, Structural and Multidisciplinary Optimization, 49 (2014) 121-129.

[35] C. Jiang, B.Y. Ni, X. Han, Y.R. Tao, Non-probabilistic convex model process: a new method of time-variant uncertainty analysis and its application to structural dynamic reliability problems, Computer Methods in Applied Mechanics and Engineering, 268 (2014) 656-676.

[36] L. Wang, X.J. Wang, Y.L. Li, J.X. Hu, A non-probabilistic time-variant reliable control method for structural vibration suppression problems with interval uncertainties, Mechanical Systems and Signal Processing, 115 (2019) 301-322.

[37] V. Dubourg, B. Sudret, J.M. Bourinet, Reliability-based design optimization using kriging surrogates and subset simulation, Structural and Multidisciplinary Optimization, 44 (2011) 673-690.

[38] T. Fang, C. Jiang, Z.L. Huang, X.P. Wei, X. Han, Time-variant reliability-based design optimization using an equivalent most probable point, IEEE Transactions on Reliability, 68 (2018) 175-186.

[39] J. Ma, P. Wriggers, W. Gao, J.J. Chen, S. Sahraee, Reliability-based optimization of trusses with random parameters under dynamic loads, Computational Mechanics, 47 (2011) 627-640.

[40] X. Jiang, Z.Z. Lu, L. Wang, Y.S. Hu, Time-dependent sequential optimization and possibility assessment method for time-dependent failure possibility-based design optimization, Aerospace Science and Technology, 110 (2021) 106492.

[41] S. Yu, Z.L. Wang, A general decoupling approach for time-and space-variant system reliability-based design optimization, Computer Methods in Applied Mechanics and Engineering, 357 (2019) 112608.

[42] Z. Meng, J.Y. Zhao, C. Jiang, An efficient semi-analytical extreme value method for time-variant reliability analysis, Structural and Multidisciplinary Optimization, (2021) 1-12.

[43] K. Sherif, W. Witteveen, K. Puchner, H. Irschik, Efficient topology optimization of large dynamic finite element systems using fatigue, Aiaa Journal, 48 (2010) 1339-1347.

[44] C. Yang, K. Liang, X.P. Zhang, Strategy for sensor number determination and placement

optimization with incomplete information based on interval possibility model and clustering avoidance distribution index, Computer Methods in Applied Mechanics and Engineering, 366 (2020) 113042.

[45] C. Yang, An adaptive sensor placement algorithm for structural health monitoring based on multi-objective iterative optimization using weight factor updating, Mechanical Systems and Signal Processing, 151 (2021) 107363.

[46] L. Wang, Q. Ren, Y.J. Ma, D. Wu, Optimal maintenance design-oriented nonprobabilistic reliability methodology for existing structures under static and dynamic mixed uncertainties, IEEE Transactions on Reliability, 68 (2018) 496-513.

[47] Y.R. Liu, L. Wang, K.X. Gu, A support vector regression (SVR)-based method for dynamic load identification using heterogeneous responses under interval uncertainties, Applied Soft Computing, (2021) 107599.

[48] C. Jiang, X.P. Wei, Z.L. Huang, J. Liu, An outcrossing rate model and its efficient calculation for time-dependent system reliability analysis, Journal of Mechanical Design, 139 (2017).

[49] L. Wang, C. Xiong, A novel methodology of sequential optimization and non-probabilistic time-dependent reliability analysis for multidisciplinary systems, Aerospace Science and Technology, 94 (2019) 105389.

[50] N.L. Pedersen, Maximization of eigenvalues using topology optimization, Structural and Multidisciplinary Optimization, 20 (2000) 2-11.

[51] M. Bruyneel, P. Duysinx, Note on topology optimization of continuum structures including self-weight, Structural and Multidisciplinary Optimization, 29 (2005) 245-256.

[52] J.H. Zhu, W.H. Zhang, P. Beckers, Integrated layout design of multi‐component system, International journal for numerical methods in engineering, 78 (2009) 631-651.

[53] L. Wang, C. Xiong, X.J. Wang, Y.L. Li, M.H. Xu, Hybrid time-variant reliability estimation for active control structures under aleatory and epistemic uncertainties, Journal of Sound and Vibration, 419 (2018) 469-492.

[54] S.O. Rice, Mathematical analysis of random noise, The Bell System Technical Journal, 23 (1944) 282-332.

[55] C. Andrieu-Renaud, B. Sudret, M. Lemaire, The PHI2 method: a way to compute

time-variant reliability, Reliability Engineering and System Safety, 84 (2004) 75-86.

[56] C. Jiang, X. Han, W.X. Li, J. Liu, Z. Zhang, A hybrid reliability approach based on probability and interval for uncertain structures, Journal of Mechanical Design, 134 (2012) 31001.

[57] L. Wang, D.L. Liu, Y.W. Yang, X.J. Wang, Z.P. Qiu, A novel method of non-probabilistic reliability-based topology optimization corresponding to continuum structures with unknown but bounded uncertainties, Computer Methods in Applied Mechanics and Engineering, 326 (2017) 573-595.